2017

# Steady 10Be-derived Paleoerosion Rates across the Plio-Pleistocene Climate Transition, Fish Creek-Vallecito Basin, California

M. E. Oskin

N. E. Longinotti

T. C. Peryam

R. J. Dorsey

C. J. DeBoer
*Western Washington University*

***See next page for additional authors***



## Recommended Citation

Oskin,M.E.,N.E.Longinotti,T. C. Peryam, R. J. Dorsey, C. J. DeBoer,B. A. Housen, and K. D. Blisniuk (2017),Steady10Be-derived paleoerosionrates across the Plio-Pleistoceneclimate transition, Fish Creek-Vallecitobasin, California, J. Geophys.Res. Earth Surf., 122, 1653–1677,doi:10.1002/2016JF004113.

AGU PUBLICATIONS

JGR

Journal of Geophysical Research: Earth Surface

RESEARCH ARTICLE

10.1002/2016JF004113

**Key Points:**

- $^{10}$Be-derived paleoerosion rates are measured from fluvial sedimentary rocks
- No change in erosion rate of eastern Peninsular Range, California, detected from 4 Ma to 1 Ma
- Plio-Pleistocene climate change had no clear effect on erosion rates in this nonglaciated setting

**Supporting Information:**

- Supporting Information S1
- Text S1
- Table S1
- Data Set S1
- Data Set S2

**Correspondence to:**
M. Oskin,
meoskin@ucdavis.edu

**Citation:**
Oskin, M. E., N. E. Longinotti, T. C. Peryam, R. J. Dorsey, C. J. DeBoer, B. A. Housen, and K. D. Blisniuk (2017), Steady $^{10}$Be-derived paleoerosion rates across the Plio-Pleistocene climate transition, Fish Creek-Vallecito basin, California, *J. Geophys. Res. Earth Surf.*, *122*, 1653–1677, doi:10.1002/2016JF004113.

Received 19 OCT 2016
Accepted 15 AUG 2017
Accepted article online 22 AUG 2017
Published online 18 SEP 2017



# Steady $^{10}$Be-derived paleoerosion rates across the Plio-Pleistocene climate transition, Fish Creek-Vallecito basin, California

**M. E. Oskin[1], N. E. Longinotti[1], T. C. Peryam[2], R. J. Dorsey[2], C. J. DeBoer[3], B. A. Housen[3], and K. D. Blisniuk[4]**

[1]Department of Earth and Planetary Sciences, University of California, Davis, California, USA, [2]Department of Geological Sciences, University of Oregon, Eugene, Oregon, USA, [3]Department of Geology, Western Washington University, Bellingham, Washington, USA, [4]Department of Geology, San Jose State University, San Jose, California, USA

**Abstract** Rates of erosion over time provide a valuable tool for gauging tectonic and climatic drivers of landscape evolution. Here we measure $^{10}$Be archived in quartz sediment from the Fish Creek-Vallecito basin to resolve a time series of catchment-averaged erosion rates and to test the hypothesis that aridity and increased climate variation after approximately 3 Ma led to an increase in erosion rates in this semiarid, ice-free setting. The Fish Creek-Vallecito basin, located east of the Peninsular Ranges in Southern California, is an ideal setting to derive a Plio-Pleistocene paleoerosion rate record. The basin has a rapid sediment accumulation rate, a detailed magnetostratigraphic age record, and its stratigraphy has been exposed through recent, rapid uplift and erosion. A well-defined source region of uniform lithology and low erosion rate provides a high, reproducible $^{10}$Be signal. We find that paleoerosion rates were remarkably consistent between 1 and 4 Ma, averaging $38 \pm 24$ m/Myr ($2\sigma$). Modern catchment-averaged erosion rates are similar to the paleoerosion rates. The uniformity of erosion over the past 4 Myr indicates that the landscape was not significantly affected by late Pliocene global climate change, nor was it affected by a local long-term increase in aridity.

## 1. Introduction

It is widely agreed that climate and tectonics both play a role in rates of erosion, but the extent and patterns of each effect are debated [*Molnar and England*, 1990; *Raymo and Ruddiman*, 1992; *Whipple and Tucker*, 1999; *Willett*, 1999; *Zhang et al.*, 2001; *Molnar*, 2004; *Finnegan et al.*, 2008; *Willenbring and von Blanckenburg*, 2010; *Herman et al.*, 2013]. Because paleoerosion rate records are difficult to directly measure, sedimentation rates have been used as a proxy [*Zhang et al.*, 2001; *Hay et al.*, 1988]. For example, *Hay et al.* [1988] identified a post-5 Ma increase in accumulation rates for terrigenous sedimentary deposits in ocean basins worldwide, hypothesized to record a global increase in erosion rates due to the effects of global cooling and increased climate variability after ~3 Ma [*Zhang et al.*, 2001; *Molnar*, 2004]. However, limitations exist for using sedimentation rates as a proxy for erosion rates. *Sadler* [1981] defined sedimentation as a discontinuous process with alternating periods of accumulation and gaps and suggested that shorter measurement intervals will tend to yield higher apparent sedimentation rates. This problem may be circumvented by spatial and temporal averaging, such as using cross-sectional measures of sedimentation rate within an appropriately closed depositional setting [*Sadler and Jerolmack*, 2015]. Unfortunately, such averaging may be difficult to achieve at the scale required to test tectonic and climate forcing of erosion of a particular landscape.

Given the limitations of the sedimentary record, the ability to measure erosion rates using $^{10}$Be provides a more direct way to test whether tectonics or climate influenced past eroding landscapes. $^{10}$Be is a cosmogenic radionuclide with a 1.39 Myr half-life ideally suited to recording the exposure history of quartz sediment [*Lal*, 1991]. The $^{10}$Be concentration of sediment integrates its entire exposure history: exhumation via erosion through the near surface, hillslope and fluvial transport, and near-surface residence during burial as a sedimentary deposit (Figure 1) [*Granger and Schaller*, 2014]. All other factors being equal, higher $^{10}$Be concentrations indicate lower erosion rates.

$^{10}$Be can be used to estimate paleoerosion rates from sedimentary strata if other sources of $^{10}$Be production can be constrained and $^{10}$Be decay can be accounted for using independently determined ages of deposits.

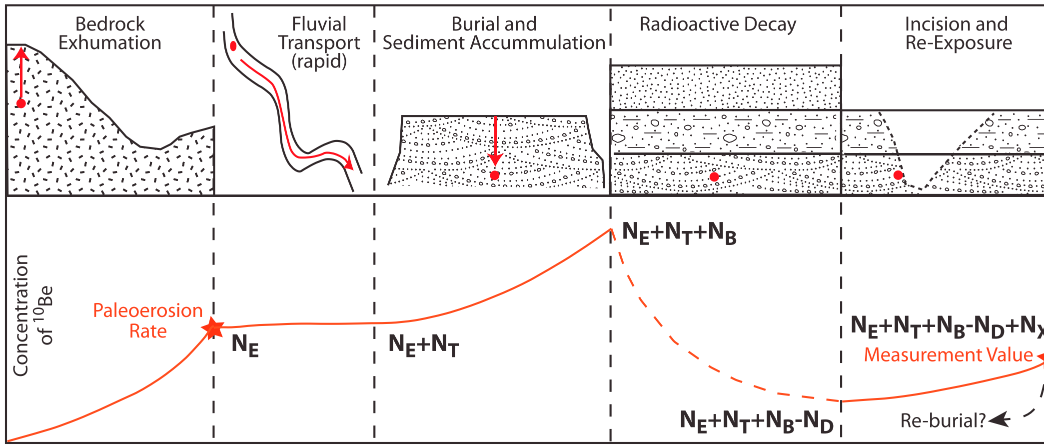


**Figure 1.** Stages of $^{10}$Be concentration acquisition and loss assuming a simple basin history. The mineral grain is exhumed toward the surface and eroded from the source rock. $N_E$ is the concentration at the time of erosion from the bedrock. The mineral grain is rapidly transported down the steep escarpment and deposited in a stream channel. The concentration acquired during transport, $N_T$, is assumed to be negligible. The mineral is rapidly buried within a channel and subsequently buried by additional channel and overbank deposits. The concentration acquired during burial is $N_B$. The mineral remains buried deeply within its depocenter for a period of time during which $^{10}$Be is lost due to decay, $N_D$. The basin sedimentary rocks are uplifted and eroded, reexposing the mineral grain. The concentration acquired during reexposure is $N_X$, and the measured concentration from sample analysis, which results from all components of $^{10}$Be ingrowth and decay, is $N_A$. Sediments may undergo multiple cycles of erosion and reburial. Proximity of the FCVB to the sediment source avoids this issue.

$^{10}$Be is commonly used to study erosion rates in modern catchment systems [e.g., *Brown et al.*, 1995, 1998; *Granger et al.*, 1996; *Riebe et al.*, 2001]. However, few studies have applied these techniques to ancient sedimentary deposits due to the difficulty of isolating precursor $^{10}$Be ingrowth from later sediment exposure history. Of the few paleoerosion rate studies published [*Granger and Schaller*, 2014], some use depositional environments where sedimentation is episodic. For example, *Granger et al.* [1997] used two cosmogenic isotopes, $^{10}$Be and $^{26}$Al, from cave sediments to simultaneously constrain sediment age and paleoerosion rate [see also *Granger et al.*, 2001; *Stock et al.*, 2004; *Refsnider*, 2010]. Fluvial deposits in river terraces have also been analyzed for paleoerosion rates [*Schaller et al.*, 2002, 2004]. Use of continuous sedimentary sections is rare because the sediment must be well dated and have undergone rapid transport and burial from a well-defined source area. *Balco and Stone* [2005] used recently exposed alluvial sediment with ages constrained by ash beds. *Charreau et al.* [2011] derive paleoerosion rates from a continuously deposited sedimentary record in the foreland of the Tian Shan, dated by magnetostratigraphic analysis. They identify a transient increase in paleoerosion rate at the onset of Northern Hemisphere continental glaciation approximately 2.5 Ma to 1.7 Ma, which they attribute to glacial modification of the sediment source region. However, follow-up studies of more sections in central Asia did not replicate this result [*Puchol et al.*, 2017]. *Val et al.* [2016] used paleoerosion rates from sediments exposed within the Argentine Precordillera convergent belt to show how the dynamics of river incision introduce lag between tectonic uplift and erosional response.

Here we develop a continuous, $^{10}$Be-derived paleoerosion record from a rift-flank setting in southernmost California to test drivers of erosion and deposition within a closely linked, source-to-sink system. The Fish Creek-Vallecito basin (FCVB) formed within the Gulf of California transtentional regime [*Axen and Fletcher*, 1998], with a history of rapid subsidence and continuous sedimentation between approximately 8 and 1 Ma [*Winker and Kidwell*, 1996; *Dorsey et al.*, 2011; *Peryam et al.*, 2011]. The adjacent footwall uplift, forming the eastern Peninsular Ranges (Figure 2), provides a well-defined and nearly monolithologic sediment source region with modest erosion rates, yielding a high $^{10}$Be signal. A steep escarpment formed along the West Salton Detachment fault separates this source region from the basin [*Shirvell et al.*, 2009], ensuring rapid sediment transport to the site of deposition with minimal $^{10}$Be ingrowth. Sediment is eroded from the upland source region and transported by bedrock channels into gorges that funnel the sediment into the FCVB. Inversion and uplift of the basin within the past 1.2 Myr [*Dorsey et al.*, 2012] has exhumed the entire sedimentary section and provided direct access to the previously buried stratigraphic section for sample collection (Figure 3).

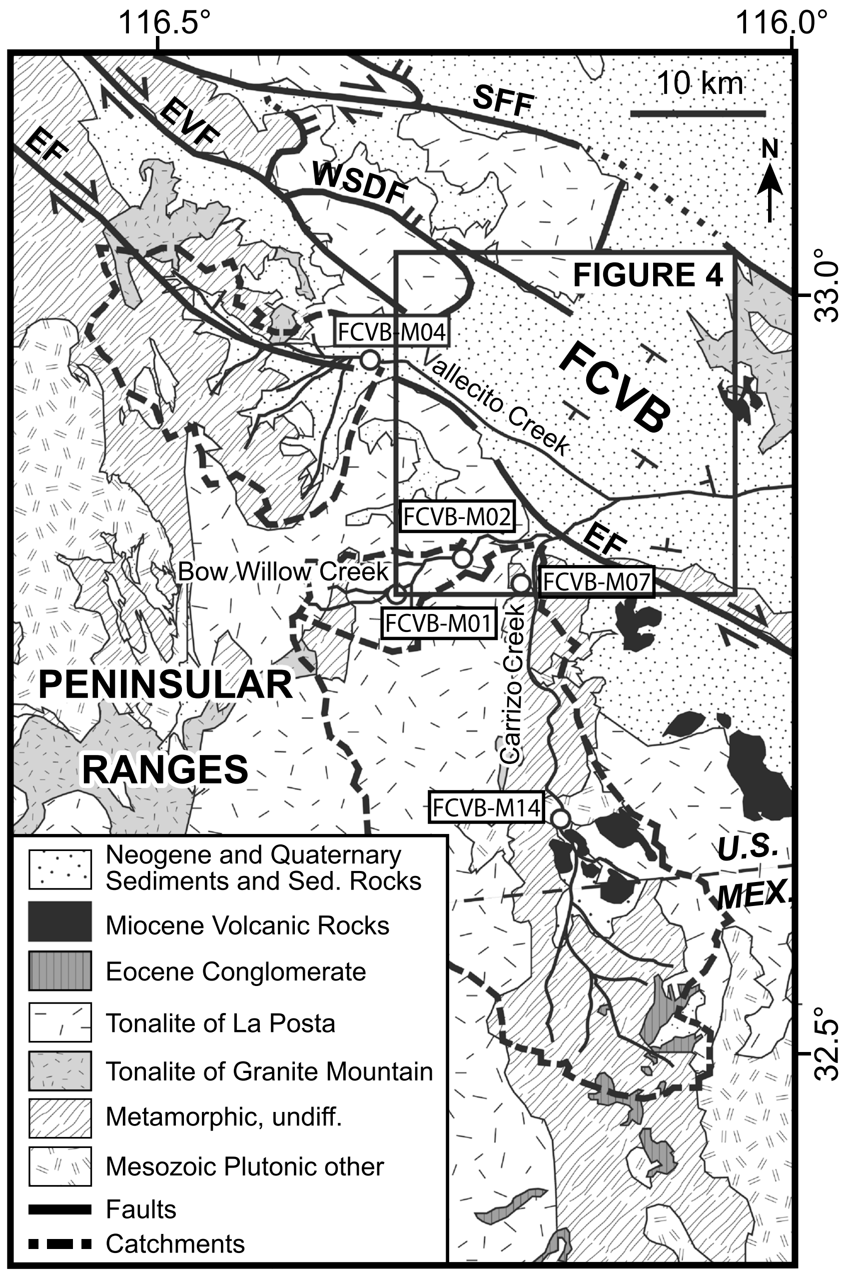


**Figure 2.** Major catchments that provided sediment to the FCVB, and source-area lithology of the eastern Peninsular Ranges of Southern California and northern Baja California. Detrital $^{10}$Be sample locations from modern streams labeled. Bow Willow Creek is a separately sampled tributary of Carrizo Creek. EF: Elsinore fault; EVF: Earthquake Valley fault; SFF: San Felipe fault; WSDF: West Salton Detachment fault.

This study analyzes $^{10}$Be from quartz sand in sedimentary rocks in the FCVB to document catchment-averaged erosion rates in its sediment source region. We develop sample extraction and processing protocols to minimize the effects of $^{10}$Be ingrowth during sediment burial and recent exhumation, yielding a robust paleoerosion rate record. Age of the sediments is independently constrained using detailed magnetostratigraphic sections assembled from *Dorsey et al.* [2011] and new measurements. To show reproducibility of paleoerosion rates, we sampled sediments derived from independent northern and southern source regions identified on the basis of clast provenance.

Stratigraphic studies in the FCVB document a decrease in sediment accumulation rate from the Pliocene to Pleistocene [*Johnson et al.*, 1983; *Dorsey et al.*, 2011], along with an abrupt progradation of locally derived

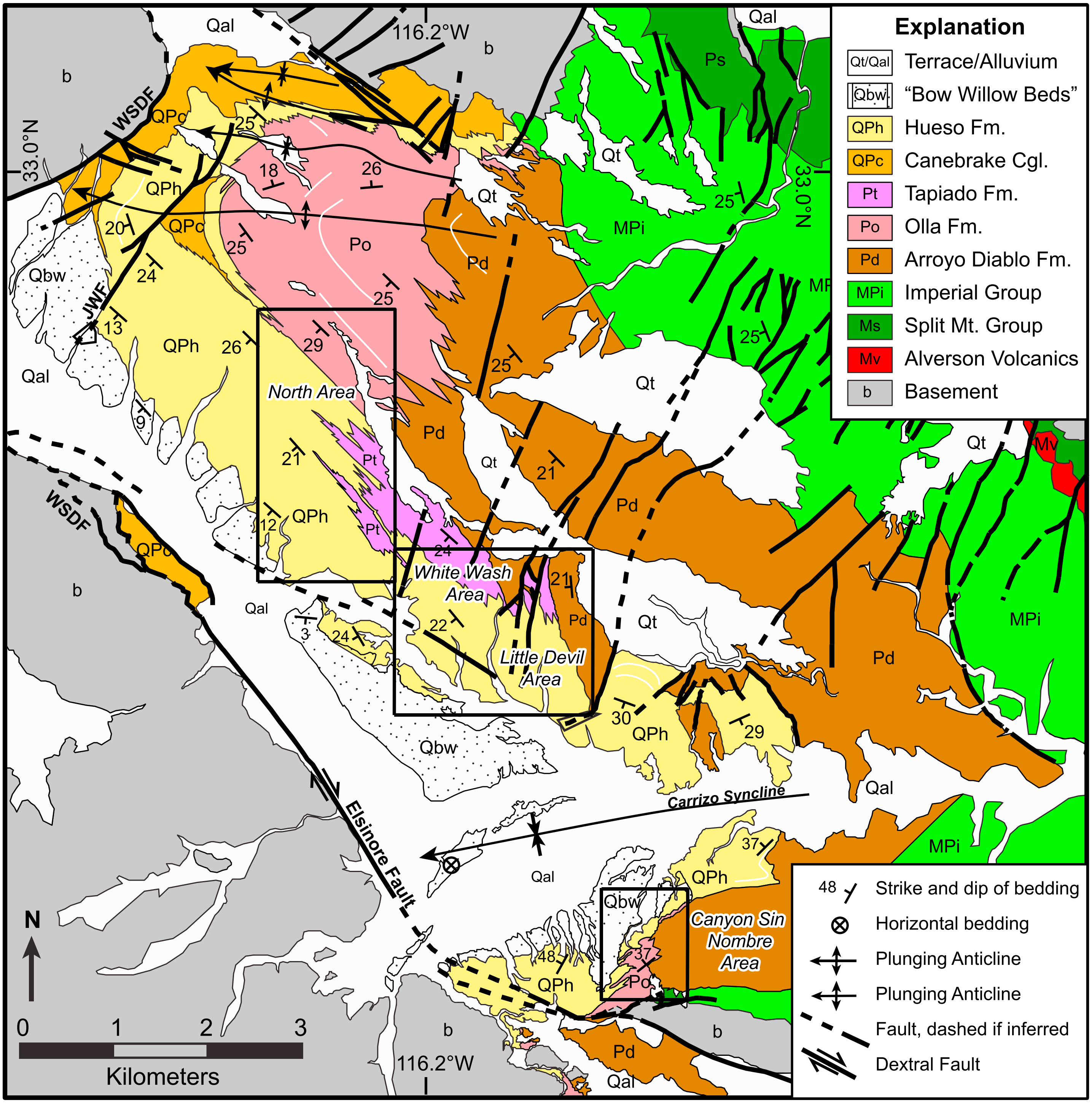


**Figure 3.** Generalized geologic map of the Fish Creek-Vallecito basin. Sedimentary rock units described in Table 2. See Figure 6 for detail of North, White Wash/Little Devil, and Canyon Sin Nombre map areas.

sediment into the basin approximately 2.8 Ma [*Dorsey et al.*, 2011; *Peryam et al.*, 2011]. This widespread pulse of progradation suggests that either the basin underwent a decrease in the rate of generation of accommodation space, or the local sediment source area experienced an increase in erosion rate that could correspond with the hypothesized change in climate variability at ~3 Ma, or the onset of tectonic footwall uplift. In order to test these hypotheses, we measure a time series of paleoerosion rate from sediments archived within the FCVB from 4 Ma, prior to the progradation event, to the youngest available section, deposited at 1 Ma.

**Table 1.** Explanation of Symbols

| Symbol | Explanation | Origin of Values |
|---|---|---|
| | *$^{10}$Be Concentrations* | |
| $N_A$ | Sample concentration | Measured |
| $N_X$ | Sample exhumation component | Calculated |
| $N_D$ | Radioactive decay component | Calculated |
| $N_B$ | Burial component | Calculated |
| $N_T$ | Sediment transport component | Assumed $\approx 0$ |
| $N_E$ | Paleoerosion rate component | Calculated |
| $\varepsilon_A$ | Sample concentration error | Measured |
| $\varepsilon_X$ | Exhumation component error | Calculated |
| $\varepsilon_D$ | Radioactive decay component error | Calculated |
| $\varepsilon_B$ | Burial component error | Calculated |
| $\langle\varepsilon\rangle$ | Compounded error of paleoerosion rate components | Calculated |
| | *Lengths, Ages, and Rates* | |
| $z$ | Excavated depth of sample | Measured |
| $y$ | Paleochannel thickness | Measured |
| $t$ | Age of sample | Stratigraphic position |
| $R_B$ | Sample burial rate | Sedimentation rate |
| $R_E$ | Paleoerosion rate | Calculated |
| $R_X$ | Sample exhumation rate | Estimated 1.5 mm/yr |
| $\delta_z$ | Excavated depth error | Measured |
| $\delta_y$ | Paleochannel thickness error | Measured |
| $\delta_t$ | Age error | Stratigraphic position |
| $\delta_B$ | Sample burial rate error | Assumed 50% or 25% |
| $\varepsilon_E$ | Paleoerosion rate error | Calculated |
| $\delta_x$ | Exhumation rate error | Estimated 1.0 mm/yr or 0.5 mm/yr |
| | *Cosmogenic Production Rate Parameters* | |
| $P_0$ | $^{10}$Be production at a site | CRONUS calculator |
| $P_B$ | $^{10}$Be production during burial | Assumed 4 atoms/g/yr |
| $P_E$ | $^{10}$Be production during erosion | Assumed 7 atoms/g/yr |
| $\rho_s$ | Density of sedimentary rocks | Assumed 2.0 g/cm$^3$ |
| $\rho_r$ | Density of basement rocks | Assumed 2.7 g/cm$^3$ |
| $\lambda$ | $^{10}$Be decay constant | $4.997 \times 10^{-7} yr^{-1}$ |
| $\Lambda$ | Mean free path for neutron spallation, slow and fast muon reactions | 160, 1500, or 5300 g/cm$^2$ |

## 2. Background

### 2.1. $^{10}$Be Applied to Paleoerosion Rates

In mineral grains near Earth's surface, cosmogenic $^{10}$Be is produced in quartz primarily via high-energy cosmic ray bombardment, resulting in the spallation of O and Si nuclei [*Cerling and Craig*, 1994]. Spallogenic $^{10}$Be production has a short attenuation mean free path ($\Lambda = \sim 160$ g/cm$^2$, see Table 1 for a full list of symbols). Thus, spallogenic production decreases quickly within ~2 m of the surface [*Lal*, 1991]. $^{10}$Be is also produced by negative (slow) muon capture and fast muon-induced reactions [*Heisinger et al.*, 2002a, 2002b]. However, nucleon spallation is the dominant $^{10}$Be production method at and near the surface, generating ~98.15% of the reactions [*Heisinger et al.*, 2002a, 2002b; *Braucher et al.*, 2003]. Slow muon production is only ~1.2% of production at the surface but has a longer mean free path ($\Lambda = \sim 1500$ g/cm$^2$) and so dominates at depths greater than 3 m below the surface [*Heisinger et al.*, 2002a, 2002b]. Fast muon reactions account for only ~0.65% of $^{10}$Be-producing reactions at the surface but dominate production at greater that 5 m depth ($\Lambda = \sim 5300$ g/cm$^2$) [*Braucher et al.*, 2003].

The production of $^{10}$Be near the surface of the earth, summed over each of these production pathways, is modeled as an exponential function of depth [*Lal*, 1991],

$$P = \sum_{j=1}^{3} P_{0,j} e^{-z\rho/\Lambda_j}, \tag{1}$$

where $P_{0,j}$ (at/g/yr) is the surface production rate for pathway $j$, $z$ (cm) is the depth below the surface, and $\rho$ (g/cm$^3$) is the density of the target. For simplicity, subsequent equations drop the summation over production pathways, though all three pathways were employed in the calculations (see supporting information Text S1 for calculation code). The cosmogenic radionuclide surface production rate varies with latitude, altitude, and over time [*Lal*, 1991; *Stone*, 2000; *Dunai*, 2000; *Desilets and Zreda*, 2003; *Desilets et al.*, 2006; *Lifton et al.*, 2014].

The concentration of cosmogenic $^{10}$Be records the lifetime of mineral grains near the surface. A low concentration of $^{10}$Be in a mineral translates to a short surface exposure time, and if the sediment is collected in a modern transport system a low concentration implies a fast erosion rate in its source region. Under the assumptions of a steady erosion rate and uniformly rapid sediment transport, the concentration of $^{10}$Be, $N_E$, in a sample of fluvial sand may be converted to an erosion rate by replacing depth, $z$, in equation (1) with the product of time, $t$, and erosion rate, $R_E$ [*Lal*, 1991; *Brown et al.*, 1995; *Granger et al.*, 1996]. Integrating from infinite time (and thus infinite depth) to the moment the sediment reaches the surface yields

$$R_E = \frac{\Lambda}{\rho}\left(\frac{P_0}{N_E} - \lambda\right). \tag{2}$$

For calculating catchment-averaged erosion rate it is common practice to assume $\Lambda = 160$ g/cm$^2$ for 100% of $^{10}$Be produced, because spallation dominates. For sufficiently rapid erosion rates (>0.001 m/kyr) the decay constant, $\lambda$, has little effect on the sample concentration and may be ignored [*Brown et al.*, 1995].

The $^{10}$Be concentration of minerals buried in a sedimentary basin may record multiple stages of exposure (Figure 1) and thus, in general, provides only a minimum concentration that does not reflect the full history of the mineral grains [*Granger*, 2006]. Extensive knowledge of the geologic history and stratigraphy of the study area is thus needed to acquire meaningful $^{10}$Be paleoerosion rates. A suitable basin must exhibit the following: (1) a well-defined source area of uniform lithology and modest erosion rate, which provides a high, reproducible $^{10}$Be signal; (2) a rapid sediment accumulation rate to quickly bury the $^{10}$Be signal out of the zone of cosmogenic production; (3) a sufficiently precise age record to correct for decay of $^{10}$Be; (4) sediment young enough to preserve $^{10}$Be acquired during erosion of the source region; and (5) a method to sample the stratigraphy such as to minimize recent exposure. These conditions, if met, result in very small corrections for sediment burial, $^{10}$Be decay, and sediment reexposure, such that the original $^{10}$Be acquired during erosion of the source region may be estimated.

The sensitivity of $^{10}$Be-derived paleoerosion rates to changes to erosion rate forcing depends on time scale set by the erosion through one spallation scale depth of rock or soil [*Schaller and Ehlers*, 2006; *Godard et al.*, 2013; *Granger and Schaller*, 2014]. This scale depth is approximately 60 cm in rock with density of 2.7 g/cm$^3$. Resolving short-term fluctuations forced by climatic oscillations over 10,000 years thus requires a modestly high erosion rate (>0.1 m/kyr). Slower average erosion rates may damp out short-term fluctuations, such as glacial-interglacial transitions [*Schaller and Ehlers*, 2006; *Godard et al.*, 2013] or the impact of earthquakes on sediment yield [*West et al.*, 2014]. Similarly, a spike in erosion rate must rapidly remove at least one-scale depth to produce a resolvable decline of $^{10}$Be concentration, with recovery time set by the postperturbation erosion rate (e.g., 6000 years to erode through one-scale depth at 0.1 m/kyr). Given how short this recovery time may be, isolated pulses of erosion may be overlooked.

### 2.2. Geologic Setting of the FCVB

The FCVB, a subsidiary basin of the Salton Trough in Southern California, fulfills all the criteria necessary to isolate late Pliocene to Pleistocene paleoerosion rates using $^{10}$Be with high precision. The basin is located east of the Peninsular Ranges of southwest California and northern Baja California (Figures 2 and 3). Two well-defined sediment source regions fed sediment into the FCVB (Figure 2). The northern source area, drained by Vallecito Creek, is a third the size of the southern source area, drained by Carrizo Creek (Figure 2). Bedrock exposures at the headwaters of Vallecito Creek occur primarily along a steep erosional escarpment that transitions

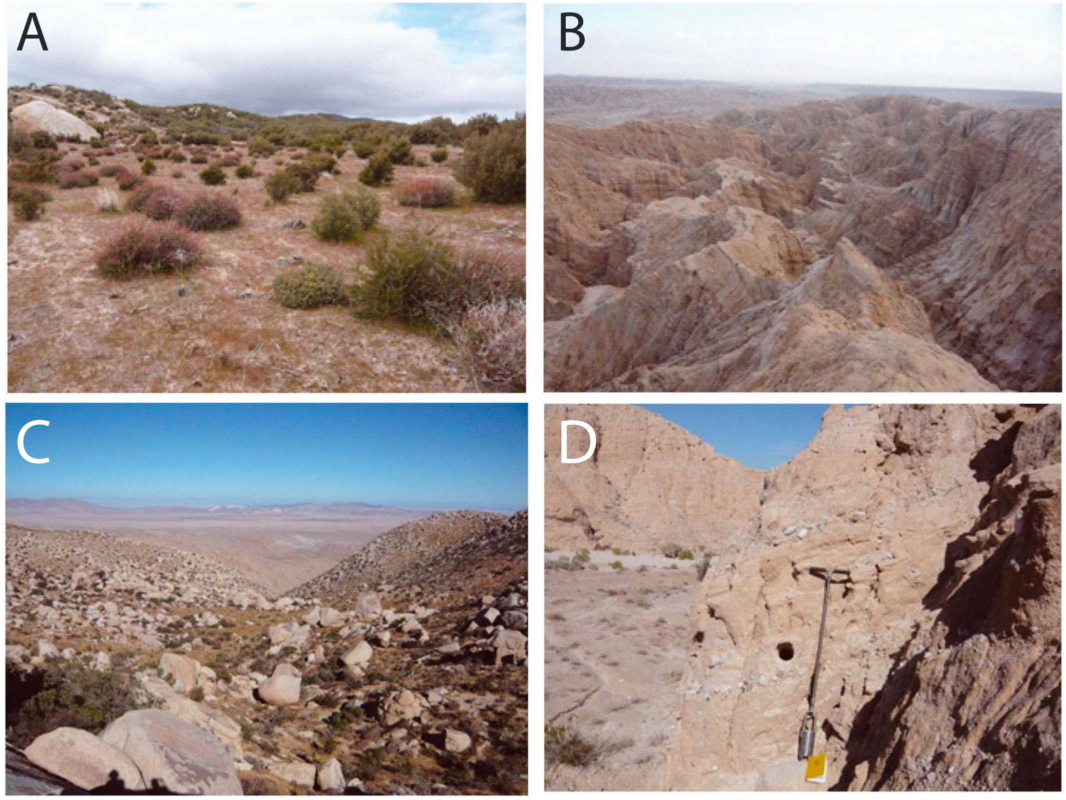


**Figure 4.** Field photographs of the FCVB and its sediment source region. (a) Typical soil-mantled landscape of an upland catchment, southern source region; (b) Badland topography formed by outcrops of southwest tilted Hueso Formation. (c) View of the FCVB from the escarpment, upper Bow Willow Creek area; (d) outcrop of a 1 m thick paleochannel, dipping gently to the left, with 1.3 m long auger for scale. Note auger hole into base of channel.

downslope into a pediment. The Carrizo Creek catchment (Figure 2) exhibits a diversity of geomorphic characteristics ranging from steep escarpments to rolling, soil-mantled uplands (Figure 4). Vegetation in these sediment source regions is dominantly mixed chaparral (mountain mahogany and scrub oak) with desert scrub at lower elevations [*Keeler-Wolf et al.*, 1998]. Although outcrops in both source regions are dominantly tonalite bedrock of Late Cretaceous age [*Todd*, 2004], rare volcanic clasts from the Jacumba volcanics and Poway conglomerate distinguish sediment sourced from the southern catchment, and metamorphosed sedimentary rocks are more abundant in the northern catchment. Preservation of the Eocene Poway conglomerate on the range crest [*Minch*, 1979] suggests a slow long-term erosion rate for the upland sediment source region.

Situated within the Pacific-North American transform plate boundary adjacent to the northernmost Gulf of California, the FCVB records a history of middle to late Miocene oblique rifting, volcanism, and marine transgression [*Winker*, 1987], late Miocene and younger detachment faulting [*Axen and Fletcher*, 1998; *Dorsey*, 2006], Pliocene to early Pleistocene subsidence and accumulation of thick marine and nonmarine deposits [*Dibblee*, 1954, 1984; *Woodard*, 1963, 1974; *Kerr*, 1984; *Winker*, 1987; *Kerr et al.*, 1991; *Dibblee*, 1996; *Winker and Kidwell*, 1996; *Dorsey et al.*, 2011; *Peryam et al.*, 2011], and early Quaternary tectonic reorganization to strike-slip faulting and shortening, which initiated uplift and erosion of the basin strata [*Johnson et al.*, 1983; *Lutz et al.*, 2006; *Kirby et al.*, 2007; *Steely et al.*, 2009; *Janecke et al.*, 2010; *Dorsey et al.*, 2012]. The Pliocene stratigraphic record preserved within the FCVB (Table 2) reveals a history of competition between local sediment sources and basin filling by the massive Colorado River Delta, which spreads across the Salton Trough from its outlet near Yuma, Arizona [*Woodard*, 1963, 1974; *Winker*, 1987; *Winker and Kidwell*, 1996; *Dorsey et al.*, 2011]. Early Pliocene Colorado River-derived marine deposits of the Imperial Group are gradually overlain by fluvial-deltaic sandstone and mudstone of the Arroyo Diablo Formation, deposited during delta progradation [*Winker*, 1987; *Winker and Kidwell*, 1996]. The Olla Formation is a unit of fluvial sandstone and mudstone derived from nearby local sources, and it interfingers laterally with Colorado River-derived deposits of the Arroyo Diablo Formation.

**Table 2.** FCVB Lithology Compiled From *Winker and Kidwell* [1996], *Dorsey et al.* [2011, 2012], and *Peryam et al.* [2011]

| Lithofacies | Lithic Designator | Description | Interpretation |
|---|---|---|---|
| Alluvium | Qal | Alluvium | Stream deposits |
| Terrace | Qt | Flat-lying capping gravels | Terrace deposits |
| Bow Willow Beds | Qbw | Gently dipping, weakly cemented sandstone, pebbly sandstone, and sandy conglomerate capped by a calcic paleoaridisol | Stream deposits, minor lacustrine limestone |
| Hueso formation | QPh | Yellow bedded sandstone: moderately sorted yellow local (L-suite) siltstone to medium-grained sandstone interbedded with moderately sorted L-suite pebbly sandstone to pebbly conglomerate | Locally derived migrating river system |
| | | Pebbly sandstone: poorly sorted medium- to coarse-grained L-suite pebbly sandstone | Distal alluvial fan |
| Canebrake Conglomerate | QPc | Clast-supported conglomerate: clast supported L-suite pebble to boulder conglomerate megabreccia: single package of clast-supported, cobble- to large boulder-breccia | Locally derived proximal alluvial fan system, rock avalanche |
| Tapiado Formation | Pt | Sandstone: medium-grained laminated to ripple cross laminated sandstone | Lake-margin |
| | | Mudstone: green to brown laminated silty L-suite claystone and argillaceous marlstone interbedded with thin beds of massive siltstone | Lacustrine |
| Olla Formation | Po | Green-bedded sandstone: green, fine-grained sandstone and mudstone | Local fluvial source |
| | | mixed: interbedded Colorado (C-suite) and local (L-suite) deposits | Mixed local fluvial and Colorado River sources |
| Arroyo Diablo Formation | Pd | Sandstone and interbedded red mudstone | Fluvial, Colorado River source |
| Imperial Group | MPi | Marine turbidites with L-suite sandstone, subaqueous sturzstrom, mudstone, and marine rhythmites | Shallow marine to delta front |
| Split Mountain Group | Ms | Lower tan sandstone member, conglomerate member, mega-breccia with a red and grey sturztrom and a larger subaerial sturzstrom | Distal to proximal alluvial fan |
| Basement | b | Biotite-hornblende tonalite, fine- to coarse-grained biotite tonalite, mylonitized biotite tonalite, quartz diorite, and metasedimentary rocks | Cretaceous plutonic and pre-Cretaceous metamorphic rock |

At ∼2.8 Ma, Colorado River input abruptly retreated within the FCVB and locally derived fluvial and pebbly sandstone of the Hueso Formation prograded across the basin [*Winker*, 1987; *Dorsey et al.*, 2011; *Peryam et al.*, 2011]. In the basin center, this basin reorganization is marked by lacustrine deposits of the Tapiado Formation. The recent, rapid uplift via folding and tilting, possibly related to slip along a restraining bend in the San Felipe fault northeast of the FCVB, began at ∼1.2 Ma and led to the cessation of sediment accumulation in the basin by ∼1 Ma [*Dorsey et al.*, 2012]. Exposure of over 5 km of continuous, tilted sedimentary section (Figure 4) in the past 1.2 Myr suggests uplift and exhumation rates well in excess of 1 mm/yr [*Dorsey et al.*, 2011]. Dextral slip on the Elsinore fault also initiated during this tectonic transition and has moved the basin a short distance to the southeast relative to the Peninsular Ranges. Correlation of crystalline bedrock and the stratigraphy of the Hueso formation both indicate <2 km translation of the FCVB from its footwall source streams via slip on the Elsinore fault [*Dorsey et al.*, 2012].

### 2.3. Testing Drivers of Sediment Progradation With $^{10}$Be

Abrupt, conformable progradation of the Hueso Formation into the FCVB at ∼2.8 Ma (Figure 3) occurred contemporaneously with a global change to a cooler, more variable climate and the onset of Northern Hemisphere glaciation [*Raymo et al.*, 1989; *Raymo*, 1994; *Clemens and Tiedemann*, 1997; *Zachos et al.*, 2001; *Ravelo et al.*, 2004; *Haug et al.*, 2005]. Locally, offshore Southern California, sea surface temperatures declined due to shoaling of the thermocline and upwelling of cooler water to the surface [*Ravelo et al.*, 2004; *Dekens et al.*, 2007]. Onshore, summer precipitation decreased and aridity increased within the FCVB [*Peryam et al.*, 2011]. This is part of a larger pattern of increased upwelling and reduction of the extent of the tropical warm-water pool toward the end of the Pliocene [*Brierley et al.*, 2009] associated with intensification of Hadley circulation [*Fedorov et al.*, 2013]. Amplified climate variation after 3 Ma [*Zachos et al.*, 2001] may especially enhance erosion and sediment export from semiarid shrubland regions, including the upper elevations of catchments draining into the FCVB, due to cyclic changes of vegetation cover [*Bull*, 1991; *Pelletier*, 2014; *Pelletier et al.*, 2016; *Dosseto and Schaller*, 2016]. Alternatively, tectonic controls may have driven the progradation. One potential mechanism is an increase in the uplift rate and topographic relief of the sediment source region, which could lead to steepening of streams and an increase in erosion rates. However, the existence of a rain shadow by approximately 2.8 Ma [*Peryam et al.*, 2011] suggests that the sediment source area to the west was already at least somewhat elevated by the time progradation began. Another tectonic mechanism is a decrease in subsidence rate of the basin, which could have driven progradation while sediment flux into the basin remained unchanged [*Paola et al.*, 1992]. Analysis of the FCVB stratigraphy by *Dorsey et al.* [2011] indeed found that subsidence rate slowed slightly before the 2.8 Ma progradation event.

Samples of quartz-bearing sediments were collected from the Hueso Formation and from beds of locally sourced sediment in the underlying Olla Formation (Table 3). The age of the $^{10}$Be samples was constrained using three detailed magnetostratigraphic transects: North, Little Devil/White Wash, and the Canyon Sin Nombre (Figure 5). The North paleomagnetic transect, published by *Dorsey et al.* [2011], expanding on earlier work by *Opdyke et al.* [1977], *Johnson et al.* [1983], and *Dorsey et al.* [2007], sampled sediment largely derived from the northern source area. The Little Devil/White Wash and Canyon Sin Nombre transects sampled sediment derived from the southern source area. Two transects were necessary for the southern source area due to discontinuous exposures of the Hueso and Olla formations across the axis of the west plunging Carrizo syncline (Figure 3). The Canyon Sin Nombre transect, located on the southern, north dipping limb of the syncline, has exposures of older sediment. All paleomagnetic sections sampled the stratigraphy at ∼10 m intervals, with more closely spaced samples near reversals. Sample polarities were determined by progressive demagnetization (Figure 6) and matched to the global magnetic polarity reference scale (Figures 7 and 8) [*Gradstein*, 2013]. Two airfall tuffs interbedded in the Tapiado formation, dated $2.60 \pm 0.06$ Ma and $2.65 \pm 0.05$ Ma, *Dorsey et al.* [2011] define the top of the Gauss normal polarity interval, enabling correlation of the North and Little Devil/White Wash sections to the reference time scale. The Canyon Sin Nombre section is tied to the time scale by geologic mapping and tested by consistency of sedimentation rates with areas to the north. Long-term sediment accumulation rates (uncorrected for compaction) were calculated from stratigraphic thickness measurements divided by time between reversals. Some of the short-duration polarity zones (<80 kyr) do not provide a reliable average and were not used in calculating accumulation rates. The North transect averaged an accumulation rate of 0.6 mm/yr after 3.1 Ma [*Dorsey et al.*, 2011]. Prior to 3.1 Ma the accumulation rate averages 2.2 mm/yr. The accumulation rate for sediment derived from the southern source changed from a more rapid 1.0 mm/yr in the older, 3–4 Ma strata to 0.7 mm/yr in the younger 2–3 Ma strata.

**Table 3.** $^{10}$Be Sample Location and Analysis Results, Grouped by Northern Source, Southern Source, and Modern Streams

| Sample | Easting (m) | Northing (m) | Elevation (m) | Mass (g) | $^{10}Be/^{9}Be$ ($\times 10^{-15}$) | Error ($\times 10^{-15}$) | $^{9}$Be Carrier (mg) | $^{10}$Be (Atom/g) | $^{10}$Be Error (Atom/g) |
|---|---|---|---|---|---|---|---|---|---|
| FCVB-02 | 573,585 | 3,642,860 | 327 | 34.68 | 63.45 | 3.37 | 0.3373 | 41,284 | 4,379 |
| FCVB-03 | 571,834 | 3,643,647 | 308 | 34.37 | 107.90 | 4.26 | 0.3552 | 74,605 | 5,891 |
| FCVB-04 | 574,191 | 3,643,507 | 297 | 93.43 | 172.94 | 6.77 | 0.3304 | 40,924 | 3,206 |
| FCVB-05 | 574,191 | 3,643,507 | 297 | 47.59 | 139.24 | 32.45 | 0.3212 | 62,889 | 29,312 |
| FCVB-08 | 572,952 | 3,644,213 | 306 | 53.33 | 45.28 | 3.13 | 0.3294 | 18,712 | 2,589 |
| FCVB-09 | 572,935 | 3,644,207 | 305 | 84.02 | 107.24 | 5.88 | 0.3299 | 28,172 | 3,089 |
| FCVB-11 | 572,919 | 3,644,213 | 306 | 74.45 | 91.98 | 5.08 | 0.3289 | 27,186 | 3,005 |
| FCVB-12 | 572,891 | 3,644,154 | 308 | 71.49 | 263.54 | 7.01 | 0.3432 | 84,659 | 4,503 |
| FCVB-13 | 572,870 | 3,644,144 | 311 | 44.20 | 74.36 | 25.21 | 0.3525 | 39,674 | 26,901 |
| FCVB-16 | 571,767 | 3,648,552 | 436 | 82.25 | 39.76 | 3.98 | 0.3530 | 11,416 | 2,287 |
| FCVB-17 | 573,204 | 3,646,838 | 378 | 31.82 | 16.70 | 2.55 | 0.3204 | 11,251 | 3,432 |
| FCVB-18 | 573,169 | 3,645,908 | 359 | 85.79 | 61.37 | 19.92 | 0.3287 | 15,732 | 10,215 |
| FCVB-23 | 571,485 | 3,643,702 | 329 | 56.23 | 91.23 | 4.09 | 0.3525 | 38,268 | 3,429 |
| FCVB-24 | 572,934 | 3,644,227 | 310 | 107.11 | 135.31 | 6.20 | 0.3220 | 27,218 | 2,493 |
| FCVB-25 | 573,661 | 3,644,316 | 324 | 104.49 | 139.51 | 13.89 | 0.3375 | 30,151 | 6,002 |
| FCVB-26 | 573,710 | 3,643,525 | 277 | 109.96 | 208.71 | 8.61 | 0.3136 | 39,828 | 3,287 |
| FCVB-29 | 572,913 | 3,648,270 | 400 | 107.40 | 40.65 | 6.94 | 0.3050 | 7,725 | 2,639 |
| FCVB-30 | 572,190 | 3,648,287 | 415 | 102.09 | 33.45 | 6.02 | 0.3330 | 7,301 | 2,627 |
| FCVB-31 | 571,686 | 3,648,462 | 435 | 103.01 | 29.77 | 5.57 | 0.3083 | 5,962 | 2,231 |
| FCVB-32 | 572,457 | 3,647,360 | 404 | 47.37 | 32.95 | 5.96 | 0.3111 | 14,481 | 5,237 |
| FCVB-34 | 571,842 | 3,644,166 | 312 | 91.39 | 191.41 | 9.35 | 0.3109 | 43,569 | 4,255 |
| FCVB-36 | 571,614 | 3,643,774 | 306 | 101.81 | 261.11 | 8.29 | 0.2985 | 51,225 | 3,252 |
| FCVB-01 | 578,273 | 3,640,078 | 224 | 35.94 | 32.11 | 2.10 | 0.3540 | 21,162 | 2,761 |
| WWB-01 | 575,274 | 3,642,482 | 293 | 132.44 | 340.01 | 11.65 | 0.2206 | 37,897 | 2,597 |
| WWB-02 | 575,096 | 3,642,402 | 283 | 101.01 | 235.31 | 8.77 | 0.2365 | 36,859 | 2,748 |
| WWB-03 | 574,940 | 3,642,222 | 280 | 103.88 | 254.01 | 13.73 | 0.2320 | 37,954 | 4,102 |
| WWB-04 | 574,540 | 3,642,066 | 266 | 104.03 | 309.81 | 19.54 | 0.2319 | 46,216 | 5,830 |
| WWB-05 | 574,698 | 3,642,191 | 272 | 102.05 | 258.31 | 12.26 | 0.2324 | 39,353 | 3,736 |
| TAP-06 | 576,012 | 3,642,308 | 250 | 120.71 | 240.21 | 10.60 | 0.2323 | 30,934 | 2,731 |
| TAP-07 | 575,824 | 3,642,172 | 253 | 151.96 | 326.91 | 16.64 | 0.2307 | 33,206 | 3,380 |
| TAP-08 | 575,708 | 3,641,887 | 255 | 101.46 | 210.51 | 8.63 | 0.2545 | 35,324 | 2,897 |
| LDW-09 | 577,483 | 3,642,142 | 272 | 125.03 | 176.91 | 8.22 | 0.2533 | 23,979 | 2,228 |
| LDW-10 | 577,398 | 3,642,076 | 272 | 115.80 | 260.61 | 10.68 | 0.2530 | 38,081 | 3,122 |
| LDW-11 | 577,244 | 3,642,078 | 277 | 120.74 | 296.51 | 13.04 | 0.2532 | 41,599 | 3,660 |
| WWB-13 | 574,571 | 3,642,422 | 270 | 112.36 | 229.51 | 13.29 | 0.2531 | 34,594 | 4,005 |
| WWB-14 | 574,719 | 3,641,952 | 268 | 100.84 | 193.91 | 11.15 | 0.2547 | 32,774 | 3,768 |
| CSN-17 | 579,565 | 3,634,749 | 241 | 242.02 | 311.81 | 14.42 | 0.2538 | 21,880 | 2,024 |
| CSN-18 | 579,090 | 3,634,527 | 246 | 213.79 | 176.51 | 8.08 | 0.3247 | 17,936 | 1,643 |
| CSN-19 | 579,495 | 3,634,469 | 245 | 256.12 | 267.31 | 10.93 | 0.2549 | 17,801 | 1,456 |
| CSN-20 | 580,222 | 3,635,471 | 215 | 242.42 | 427.71 | 14.51 | 0.2539 | 29,969 | 2,034 |
| CSN-21 | 579,867 | 3,634,876 | 232 | 245.06 | 271.01 | 9.60 | 0.2530 | 18,716 | 1,326 |
| CSN-22 | 580,062 | 3,635,173 | 221 | 250.04 | 260.31 | 9.20 | 0.2527 | 17,601 | 1,243 |
| CSN-23 | 579,797 | 3,634,580 | 246 | 259.16 | 220.91 | 8.69 | 0.2528 | 14,419 | 1,134 |
| CSN-24 | 580,213 | 3,635,687 | 202 | 254.85 | 417.51 | 12.58 | 0.2535 | 27,780 | 1,675 |
| CSN-25 | 579,473 | 3,634,051 | 275 | 256.18 | 342.11 | 10.03 | 0.2533 | 22,630 | 1,326 |
| CSN-26 | 579,493 | 3,634,224 | 260 | 264.28 | 272.71 | 9.15 | 0.2533 | 17,490 | 1,174 |
| CSN-27 | 580,049 | 3,635,262 | 218 | 269.70 | 386.81 | 13.08 | 0.2520 | 24,180 | 1,635 |
| CSN-28 | 580,198 | 3,635,670 | 211 | 255.37 | 426.91 | 17.63 | 0.2518 | 28,157 | 2,326 |
| FCVB-M4 | 561,999 | 3,647,973 | 434 | 37.38 | 236.00 | 10.99 | 0.3545 | 149,754 | 13,947 |
| FCVB-M1 | 565,990 | 3,630,124 | 1162 | 97.19 | 497.14 | 10.82 | 0.3487 | 119,343 | 5,193 |
| FCVB-M2 | 570,353 | 3,632,600 | 382 | 101.78 | 444.34 | 10.06 | 0.3239 | 94,624 | 4,287 |
| FVCB-M7 | 574,036 | 3,630,941 | 262 | 58.73 | 225.64 | 28.05 | 0.3165 | 81,363 | 20,233 |
| FCVB-M14 | 572,870 | 3,644,144 | 846 | 94.23 | 499.64 | 25.29 | 0.3377 | 119,807 | 12,128 |

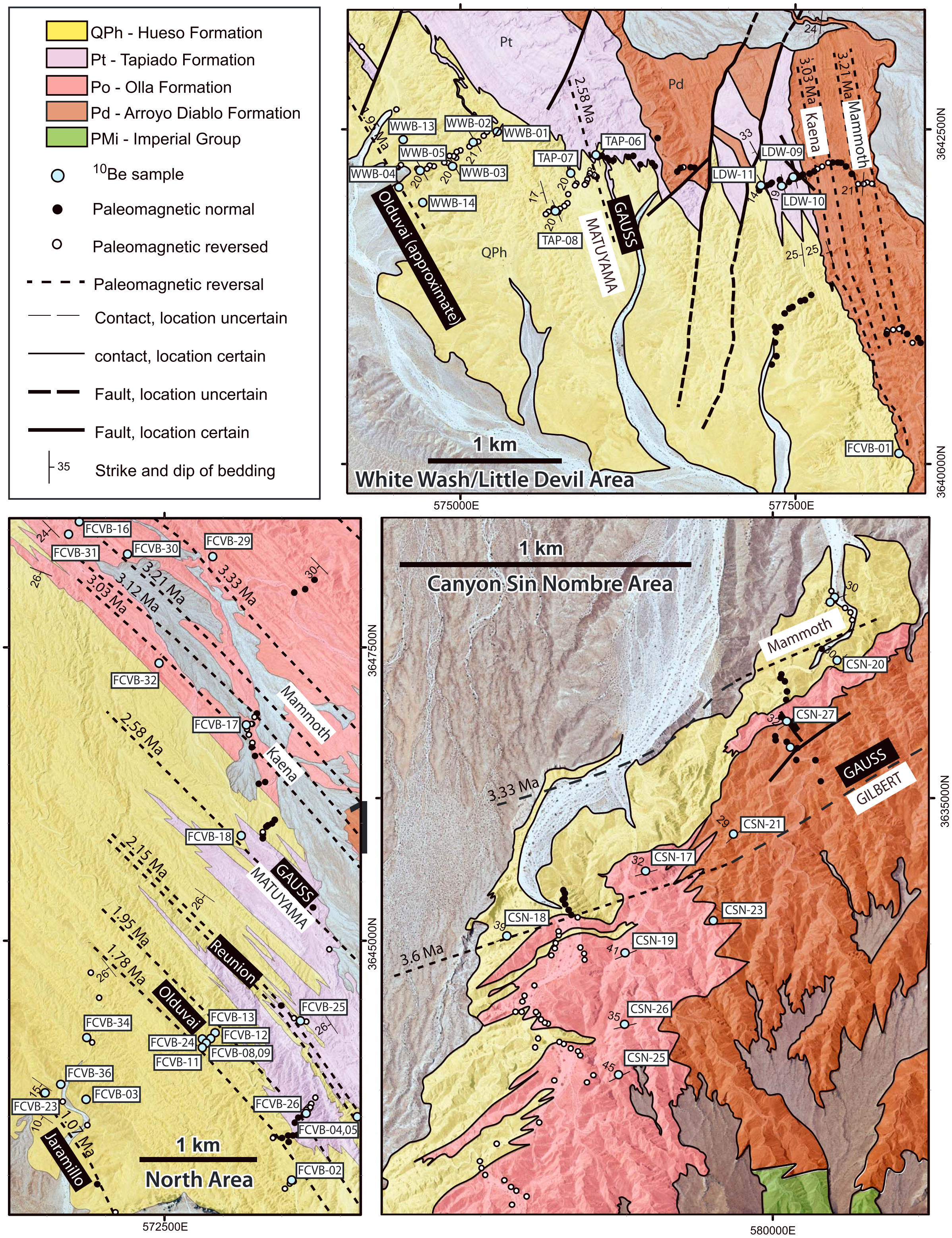


**Figure 5.** FCVB sedimentary section sample collection sites and geologic interpretation overlain on imagery from the National Aerial Imagery Program. Blue dots show locations of $^{10}$Be sample collection sites; black and white dots show paleomagnetic sample sites. Reversal locations in the stratigraphic sections are denoted by black dashed lines and labeled with ages. Named Chron boundaries (Matuyama, Gauss, and Gilbert) and subchrons labeled. Black: normal polarity; white: reversed polarity.

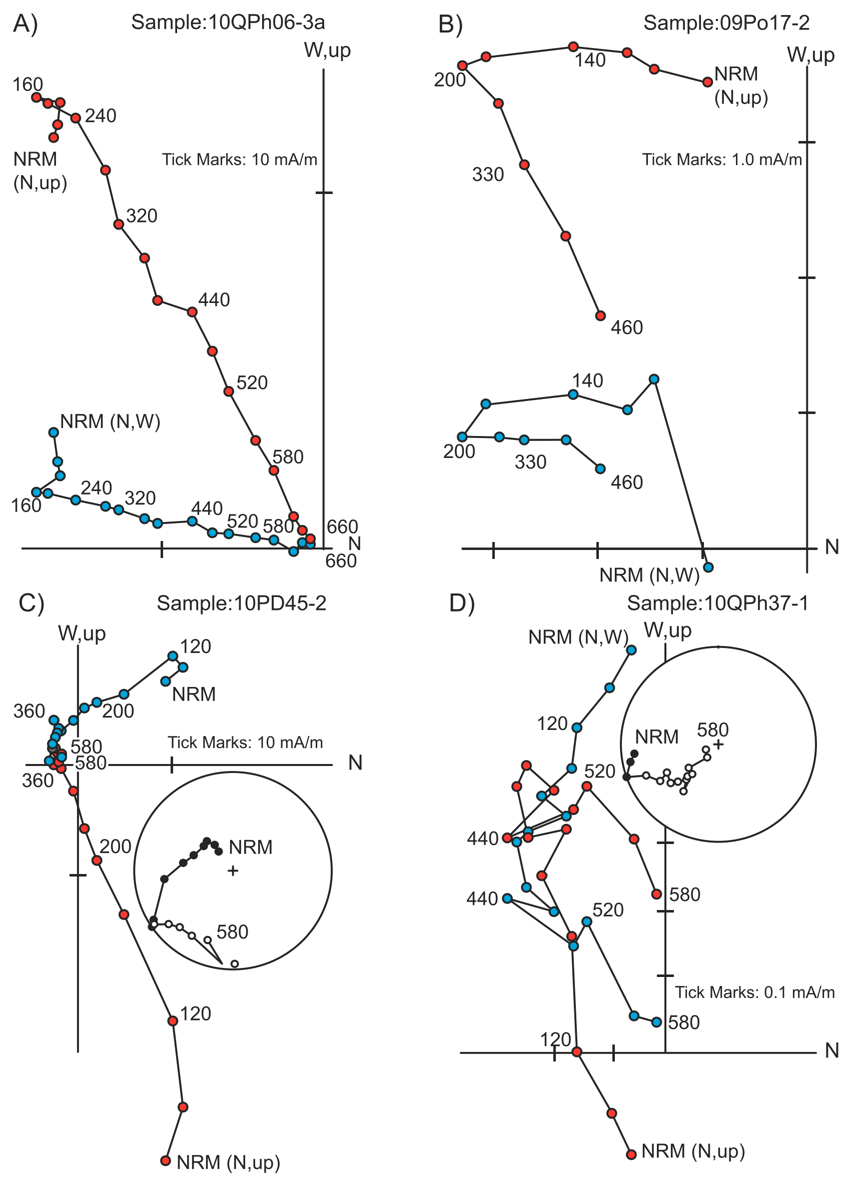


**Figure 6.** Example demagnetization paths for samples from the Hueso and Olla formations. North (N), west (W), and up are vector directions of magnetic moment per unit volume of sample, in units of milliamperes per meter. NRM is the sample natural remanent magnetism prior to stepwise demagnetization. N,up (red in color version) and N,W (blue in color version) vector components are plotted together on one set of axes. Stereonet projections for samples C and D illustrate remanence direction shifts with progressive demagnetization. Open circles are upward pointing vectors. (a) Class 1 demagnetization behavior, with well-defined linear magnetization components. (b) Class 2 demagnetization behavior—with well-defined linear components before sample failure (disaggregation) during heating. (c) Class 3 behavior, with well-defined but curvilinear components. (d) Class 4 behavior, with scattered, curvilinear components where polarity can nevertheless be defined.

Latitude and elevation both affect the $^{10}$Be production rate [*Lal*, 1991]. Although sediment sources and the FCVB lie at effectively the same latitude, 33°, the elevations vary considerably from the sediment source to sink. The northern catchment (Vallecito) has an average elevation of 923 m above sea level, while the southern catchment (Carrizo) has an average of 1036 m. The smaller Bow Willow tributary of the Carrizo catchment has the highest average elevation of 1174 m. The elevation during deposition was likely much lower than this but still above the Plio-Pleistocene sea level because the sediments are nonmarine and transition upsection from fluvial-deltaic deposits [*Dorsey et al.*, 2011]. Elevation of the basin during deposition is thus estimated to lie between sea level and 300 m. Analysis of paleosols and carbon and oxygen isotopes in the basin indicate a rain shadow was already in place between 3.7 and 1.0 Ma [*Peryam et al.*, 2011]. Thus, neither the basin nor source

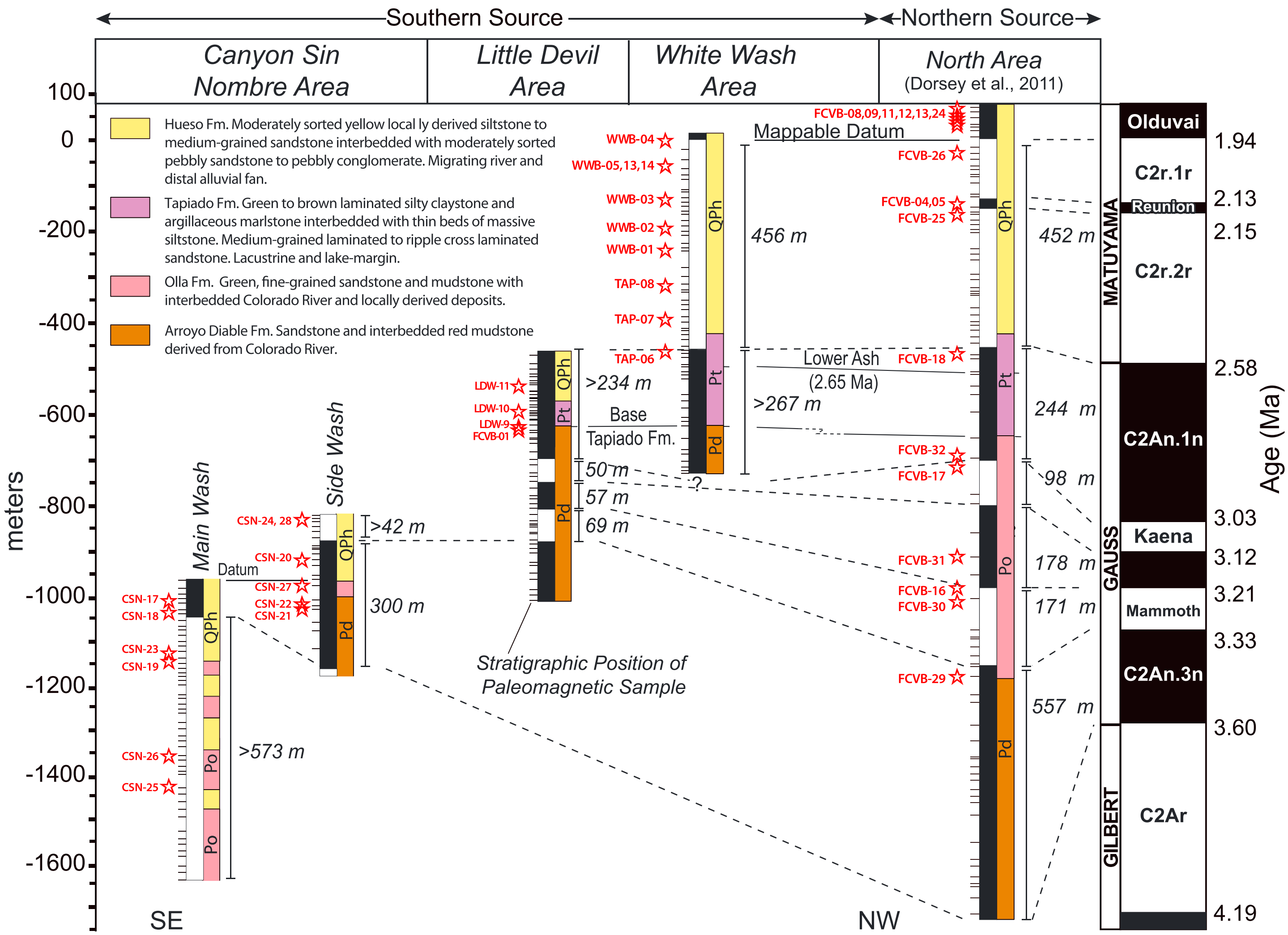


**Figure 7.** Magnetostratigraphic correlation across the FCVB, with $^{10}$Be sample locations between 1.8 and 4.0 Ma. See Figure 5 for sample location maps.

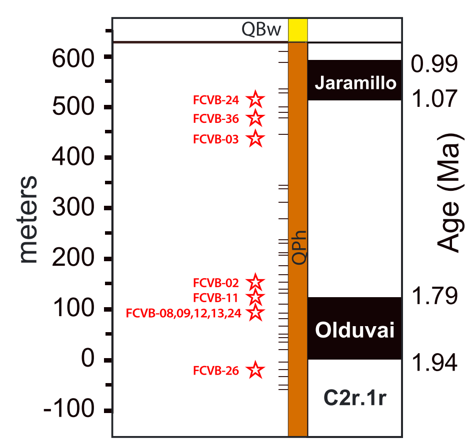


**Figure 8.** Magnetostratigraphic column and sample locations for North area between 0.9 and 2.0 Ma. See Figure 5 for sample location map.

region hypsometry appears to have changed substantially over the past 4 Myr. However, we cannot rule out a modest increase in elevation of the source region as slip accrued on the West Salton Detachment fault, and we expect a modest amount of surface lowering in the source region due to erosion. The impact of these assumptions are explored in section 5. It is further assumed that cosmogenic production rate at sea level has not varied significantly over the past 4 Myr [*Dunai*, 2001]. However, because the production rate is affected by magnetic field strength, short-term production rates will vary. This is especially important approaching magnetic reversals [*Valet et al.*, 2005], when magnetic field strength temporarily declines and cosmic ray flux increases. Where possible, we took care to sample just prior to reversals identified in the magnetostratigraphic record, before the effects of reduced magnetic field strength could impact the $^{10}$Be signal.

## 3. Methods

### 3.1. $^{10}$Be Sample Acquisition and Measurement

Sample extraction and laboratory methods were refined throughout the study as we learned how to best control for uncertainty due to ingrowth of $^{10}$Be during exhumation of the FCVB, possible increased $^{10}$Be production during magnetic reversals, and low $^{10}$Be concentrations in our oldest samples due to radioactive decay. In total, 48 sediment samples from the FCVB, along with five samples from the modern washes (Figure 3), were successfully analyzed (Table 3). Twenty two of these basin samples were collected in sediment derived from the northern catchment and 26 from sediment derived from the southern catchment. Modern wash samples were collected from the bottoms of active stream beds. Roughly, 1–3 kg of sediment from each site was collected at each location. Sedimentary basin samples were selectively collected from the bottoms of 1–4 m thick sandstone paleochannels (Figure 4). Thick channel fills ensure rapid, immediate burial at deposition and minimize exposure to cosmogenic radiation during subsequent further burial. Extraction sites ranged from deeply incised washes to isolated outcrops of sedimentary rocks. To reduce $^{10}$Be due to exhumation of the outcrop, most samples were collected by hand-augering below the outcrop surface at least 0.50 m along bedding planes. Due to the inherent episodicity of local erosion rates, samples collected from shallower depths, or from outcrop surfaces, produce more scattered, less reliable results.

Standard mechanical extraction techniques were used to isolate quartz and prepare targets for measurement of $^{10}$Be via accelerator mass spectrometry. Sand samples were crushed and sieved. Resulting 250–500 μm size fractions were chemically prepared in cosmogenic nuclide laboratories at the University of California, Santa Barbara, and Stanford University. Samples were magnetically separated, cleaned in a HCl acid bath, and leached in a minimum of three HF/$HNO_3$ acid mixtures: one high concentration leach (2%) and at least two low concentration leaches (1%). Between 35 and 270 g of purified quartz was dissolved in concentrated HF (Table 3). Early in our study we collected and processed too little sample mass from the older part of the northern section, resulting in low current yield and large analytical uncertainties for some samples. To overcome this, we used roughly double the amount of mass for the oldest samples collected in Canyon Sin Nombre to compensate for low $^{10}$Be concentration due to the antiquity of the sediment (2–3 $^{10}$Be half-lives). During quartz dissolution a known amount of in-house $^{9}$Be carrier was added to each sample (Table 3). Samples were then filtered through anion and cation exchange columns to isolate the beryllium fraction. The samples processed with more material were passed through the cation column twice. The $^{10}$Be fraction was precipitated to beryllium hydroxide and was then oxidized at 850°C. The beryllium oxide was mixed with niobium powder and loaded into steel targets. $^{10}$Be/$^{9}$Be ratios were measured at the Purdue Rare Isotope Measurement (PRIME) Laboratory, Purdue University (Table 3). The 07KNSTD standardization was used to measure $^{10}$Be concentrations and uses a $^{10}$Be half-life of 1.36 ± 0.07 Myr [*Nishiizumi et al.*, 2007]. Paleoerosion rates were corrected for $^{10}$Be decay with the newer half-life value of 1.387 ± 0.012 Myr [*Chmeleff et al.*, 2010; *Korschinek et al.*, 2010]; however, the two different half-life values do not significantly affect the resulting paleoerosion rate values.

### 3.2. Magnetostratigraphic Age Control

Paleoerosion rates require correction of present-day $^{10}$Be concentrations for radioactive decay. We utilize the well-constrained, high-resolution magnetostratigraphy of the FCVB documented by *Dorsey et al.* [2011] for age control of sediments derived from the northern source area (Figure 5). Sediment thicknesses were estimated by *Dorsey et al.* [2011] by a combination of direct measurement with a Jacob's staff, and estimates based on across-strike map distance and bedding dip. Bedding dips are highly uniform over large areas of the basin, except for a zone of fanning dips in the uppermost Hueso formation [*Dorsey et al.*, 2012]. Detailed mapping of the nearly 100% exposure of the FCVB enables us to confidently correlate this section to the Little Devil/White Wash area, where sediments from the southern source are exposed. However, more substantial faulting and folding in this area required that we measure multiple overlapping magnetostratigraphic sections in order to confidently reconstruct the reversal history. Oblique, rather than across-strike exposure in the Canyon Sin Nombre area also required overlapping transects, although here structural complications were less of a concern. The new stratigraphic sections presented here were measured with a Jacob's staff, and adjacent sections independently correlated with marker beds where available.

Sample collection methods and analysis of magnetic polarity followed the procedures described in *Dorsey et al.* [2011]. Paleomagnetic samples were collected with a portable drill, and three to seven samples were collected at each site. Sample sites were arranged closely together (~10 m apart stratigraphically) to capture polarity boundaries precisely. In total, 184 sites were collected, providing 113 and 71 new polarity determinations for the Little Devil/White Wash section and Canyon Sin Nombre section, respectively (see Table S1 in the supporting information for paleomagnetic results). Paleomagnetic samples were cut into standard-size specimens and measured at the Western Washington University paleomagnetism laboratory with a 2-G 755-R Cryogenic magnetometer. Specimens were subjected to stepwise thermal or alternating field demagnetization. For some samples both techniques were applied. Orthogonal vector plots and stereographic projections were used to determine the characteristic magnetization and magnetic polarity of the specimens and to qualitatively assess the quality of the polarity determinations at each site (Figure 6).

To determine the $^{10}$Be sample ages, the collection sites were assigned positions in the stratigraphic measured sections that were sampled for magnetostratigraphic dating (Figures 7 and 8). In the North and Little Devil/White Wash sections the thickness between $^{10}$Be sample sites and the nearest paleomagnetostratigraphic sample sites was measured in the field using a Jacob's staff. $^{10}$Be samples collected in Canyon Sin Nombre were tied into the measured section using marker beds mapped on enhanced digital orthophotos, and thicknesses were estimated using the strikes and dips recorded in the field. For each $^{10}$Be sample, the time between deposition of the sample sediment and the nearest reversal was then calculated by dividing the stratigraphic thickness between the sample site and the nearest reversal by the accumulation rate. This time value added to or subtracted from the nearest reversal age gives the sample ages. Age error was assigned based on how well correlated the location of the $^{10}$Be site was to the measured section along with confidence in the reversal location and the stratigraphic thickness of the beds between reversals. As an independent check on the magnetostratigraphic age control, the ratio of $^{26}$Al to $^{10}$Be was analyzed for many samples to determine burial ages, after correcting for ingrowth during exhumation [*Longinotti*, 2012]. Unfortunately, there proved to be too much naturally occurring $^{27}$Al in the basin samples to obtain reliable $^{26}$Al / $^{27}$Al ratios, and thus, large uncertainties made the resulting ages of little use for verifying the magnetostratigraphic ages.

### 3.3. Paleoerosion Rates

With sediment age independently constrained from magnetostratigraphy, and the earliest $^{10}$Be ingrowth isolated from the later exposure history, the $^{10}$Be catchment averaged erosion rate technique may be applied to ancient sediment using equation (2). The analyzed concentration, $N_A$, of each basin sample records multiple stages of $^{10}$Be ingrowth and decay (Figure 1). After the sediment is eroded from the source rock and transported down the hillslope, it carries a $^{10}$Be concentration, $N_E$, that is inversely proportional to the bedrock lowering rate [e.g., *Brown et al.*, 1995]. After liberation of the sediment from the hillslope to the fluvial system, the mineral grains acquire additional $^{10}$Be during transport from the upland area to the basin, $N_T$, deposition and burial in the basin, $N_B$, and exposure via exhumation of the sediments, $N_X$. Between burial and exhumation the sediment is covered by sufficient material that no additional $^{10}$Be accumulates, and instead concentration is lost due to radioactive decay, $N_D$. Due to the long sediment residence deeply buried within the basin, we separate the decay component from burial and exhumation, resulting in an overall simpler formulation and error analysis than that employed by *Charreau et al.* [2011]. The measured concentration can be thus modeled as a linear combination of five components,

$$N_A = N_E + N_T + N_B - N_D + N_X, \tag{3}$$

that we invert progressively back through time (from $N_X$ to $N_E$), compounding uncertainties from sample analysis, sample site context, and the range of permissible values of exhumation rate, sample age, and burial rate (Table 4). A buried basin sediment sample is assumed to have undergone a single erosion-deposition cycle that began with detachment from the source rock in the upland source region, followed by rapid transport off the escarpment and deposition at the bottom of a stream channel. We assume negligible $^{10}$Be acquired during transport, due to the proximity of the FCVB to the sediment source region and low sediment storage within channels [*Yanites et al.*, 2009]. We further assumed that the sediment was then rapidly buried and remained buried until the basin was recently uplifted and eroded (Figure 1).

Uncertainties associated with each of the concentration terms introduce errors with asymmetric distributions due to the exponential depth dependence of $^{10}$Be production and time dependence of decay. To compute final paleoerosion rate results, we compounded the uncertainties at each step using a Monte Carlo approach with 100,000 iterations per $^{10}$Be sample. Errors were not assigned for $^{10}$Be production rate in the sediment source area, nor for the production rate in the FCVB during deposition and sediment burial. Precise values for these rates are unknown, but we expect that these would have changed only slowly with the average

**Table 4.** $^{10}$Be Sample Analysis Parameters and Paleoerosion Rates

| Sample | Age (Myr) | $^{10}$Be (Atoms/g) | $^{10}$Be Production (Atoms/g/yr) | Excavation Depth (cm) | Channel Depth (cm) | Burial Rate (cm/yr) | Paleoerosion Rate (m/Myr) |
|---|---|---|---|---|---|---|---|
| FCVB-02 | 1.71 ± 0.03 | 41,284 ± 4,379 | 4.12 | 25.0 ± 10.0 | 350 ± 20 | 0.06 | 46 +6/−7 |
| FCVB-03 | 1.20 ± 0.05 | 74,605 ± 5,891 | 4.05 | 25.0 ± 10.0 | 200 ± 20 | 0.06 | 32 +3/−3 |
| FCVB-04 | 2.16 ± 0.01 | 40,924 ± 3,206 | 4.02 | 10.0 ± 5.00 | 130 ± 10 | 0.06 | 37 +4/−5 |
| FCVB-05 | 2.16 ± 0.01 | 62,889 ± 29,312 | 4.02 | 10.0 ± 5.00 | 130 ± 10 | 0.06 | 23 +22/−5 |
| FCVB-08 | 1.80 ± 0.03 | 18,712 ± 2,589 | 4.05 | 15.0 ± 10.0 | 170 ± 20 | 0.06 | 110 +27/−30 |
| FCVB-09 | 1.80 ± 0.02 | 28,171 ± 3,088 | 4.04 | 15.0 ± 5.00 | 170 ± 30 | 0.06 | 68 +11/−13 |
| FCVB-11 | 1.78 ± 0.02 | 27,186 ± 3,005 | 4.05 | 10.0 ± 5.00 | 350 ± 30 | 0.06 | 71 +12/−14 |
| FCVB-12 | 1.81 ± 0.03 | 84,659 ± 4,503 | 4.05 | 15.0 ± 10.0 | 130 ± 30 | 0.06 | 20 +1/−2 |
| FCVB-13 | 1.82 ± 0.04 | 39,673 ± 26,901 | 4.06 | 10.0 ± 5.00 | 180 ± 20 | 0.06 | 46+117/−20 |
| FCVB-16 | 3.20 ± 0.02 | 11,416 ± 2,287 | 4.52 | 15.0 ± 5.00 | 140±20 | 0.06 | 102 +56/−44 |
| FCVB-17 | 3.08 ± 0.01 | 11,251 ± 3,432 | 4.30 | 10.0 ± 5.00 | 130 ± 20 | 0.06 | 112+101/−51 |
| FCVB-18 | 2.60 ± 0.06 | 15,732 ± 10,215 | 4.23 | 35.0 ± 25.0 | 140 ± 20 | 0.06 | 80+267/−38 |
| FCVB-23 | 1.07 ± 0.02 | 38,268 ± 3,429 | 4.13 | 10.0 ± 5.00 | 400 ± 30 | 0.06 | 69 +8/−11 |
| FCVB-24 | 1.80 ± 0.02 | 27,218 ± 2,493 | 4.06 | 74.5 ± 8.00 | 300 ± 30 | 0.06 | 67 +8/−10 |
| FCVB-25 | 2.18 ± 0.02 | 30,151 ± 6,002 | 4.11 | 106.5 ± 7.50 | 160 ± 20 | 0.06 | 49 +13/−10 |
| FCVB-26 | 1.98 ± 0.03 | 39,828 ± 3,287 | 3.95 | 95.0 ± 10.0 | 320 ± 20 | 0.06 | 40 +4/−4 |
| FCVB-29 | 3.36 ± 0.01 | 7,725 ± 2,639 | 4.39 | 62.5 ± 7.50 | 180 ± 10 | 0.06 | 139+142/−63 |
| FCVB-30 | 3.24 ± 0.03 | 7,301 ± 2,627 | 4.44 | 70.0 ± 10.0 | 250 ± 20 | 0.06 | 156+174/−72 |
| FCVB-31 | 3.17 ± 0.03 | 5,962 ± 2,231 | 4.52 | 55.0 ± 10.0 | 300 ± 20 | 0.06 | 230+500/−128 |
| FCVB-32 | 2.99 ± 0.02 | 14,481 ± 5,237 | 4.40 | 67.5 ± 12.5 | 150 ± 20 | 0.06 | 76 +56/−27 |
| FCVB-34 | 1.38 ± 0.06 | 43,569 ± 4,255 | 4.07 | 95.0 ± 15.0 | 250 ± 20 | 0.06 | 50 +6/−6 |
| FCVB-36 | 1.15 ± 0.03 | 51,225 ± 3,252 | 4.05 | 110.0 ± 10.0 | 370 ± 30 | 0.06 | 47 +3/−4 |
| FCVB-01 | 2.91 ± 0.05 | 21,162 ± 2,761 | 3.77 | 25.0 ± 10.0 | 140 ± 5 | 0.07 | 52+10/−11 |
| WWB-01 | 2.29 ± 0.02 | 37,897 ± 2,597 | 4.00 | 61.5 ± 11.5 | 120 ± 5 | 0.07 | 37 +3/−4 |
| WWB-02 | 2.22 ± 0.02 | 36,859 ± 2,748 | 3.97 | 64.0 ± 14.0 | 140 ± 5 | 0.07 | 39 +4/−4 |
| WWB-03 | 2.12 ± 0.02 | 37,954 ± 4,102 | 3.96 | 59.0 ± 9.00 | 110 ± 5 | 0.07 | 40 +5/−6 |
| WWB-04 | 1.93 ± 0.02 | 46,216 ± 5,830 | 3.91 | 64.0 ± 14.0 | 94 ± 5 | 0.07 | 36 +5/−5 |
| WWB-05[a] | 2.01 ± 0.02 | 39,353 ± 3,736 | 3.93 | 61.5 ± 11.5 | 125 ± 5 | 0.07 | 41 +5/−5 |
| TAP-06 | 2.61 ± 0.05 | 30,934 ± 2,731 | 3.86 | 63.5 ± 13.5 | 290 ± 5 | 0.07 | 39 +4/−5 |
| TAP-07 | 2.49 ± 0.01 | 33,206 ± 3,380 | 3.87 | 60.5 ± 10.5 | 70 ± 5 | 0.07 | 39 +5/−5 |
| TAP-08 | 2.39 ± 0.01 | 35,324 ± 2,897 | 3.87 | 61.5 ± 11.5 | 140 ± 5 | 0.07 | 38 +4/−5 |
| LDW-09 | 2.90 ± 0.03 | 23,979 ± 2,228 | 3.93 | 66.0 ± 12.0 | 150 ± 5 | 0.07 | 44 +5/−7 |
| LDW-10 | 2.82 ± 0.03 | 38,081 ± 3,122 | 3.93 | 60.5 ± 10.5 | 80 ± 5 | 0.07 | 28 +3/−3 |
| LDW-11 | 2.72 ± 0.03 | 41,599 ± 3,660 | 3.95 | 62.0 ± 10.0 | 110 ± 5 | 0.07 | 27 +3/−3 |
| WWB-13[a] | 2.01 ± 0.02 | 34,594 ± 4,005 | 3.92 | 88.5 ± 15.5 | 120 ± 5 | 0.07 | 47 +7/−6 |
| WWB-14[a] | 2.01 ± 0.02 | 32,774 ± 3,768 | 3.92 | 64.0 ± 14.0 | 110 ± 5 | 0.07 | 50 +7/−7 |
| CSN-17 | 3.56 ± 0.03 | 21,880 ± 2,024 | 3.83 | 56.0 ± 6.00 | 230 ± 5 | 0.10 | 35 +4/−6 |
| CSN-18 | 3.58 ± 0.02 | 17,936 ± 1,643 | 3.84 | 62.5 ± 12.5 | 115 ± 5 | 0.10 | 43 +6/−8 |
| CSN-19 | 3.69 ± 0.01 | 17,801 ± 1,456 | 3.84 | 61.8 ± 11.8 | 100 ± 5 | 0.10 | 41 +5/−8 |
| CSN-20 | 3.36 ± 0.01 | 29,969 ± 2,034 | 3.74 | 61.8 ± 11.8 | 106 ± 5 | 0.10 | 27 +2/−3 |
| CSN-21 | 3.46 ± 0.04 | 18,716 ± 1,326 | 3.80 | 61.8 ± 11.8 | 101 ± 5 | 0.10 | 43 +5/−8 |
| CSN-22 | 3.45 ± 0.01 | 17,601 ± 1,243 | 3.76 | 58.5 ± 8.50 | 105 ± 5 | 0.10 | 47 +5/−9 |
| CSN-23 | 3.67 ± 0.02 | 14,419 ± 1134 | 3.84 | 65.0 ± 13.0 | 130 ± 5 | 0.10 | 52 +7/−11 |
| CSN-24[a] | 3.29 ± 0.01 | 27,780 ± 1,675 | 3.70 | 68.0 ± 10.0 | 196 ± 5 | 0.10 | 30 +2/−4 |
| CSN-25 | 3.92 ± 0.04 | 22,630 ± 1,326 | 3.94 | 59.3 ± 9.30 | 120 ± 5 | 0.10 | 28 +3/−4 |
| CSN-26 | 3.84 ± 0.05 | 17,490 ± 1,174 | 3.89 | 59.5 ± 9.50 | 104 ± 5 | 0.10 | 39 +5/−7 |
| CSN-27 | 3.40 ± 0.01 | 24,180 ± 1,635 | 3.75 | 62.0 ± 12.0 | 120 ± 5 | 0.10 | 34 +3/−5 |
| CSN-28[a] | 3.29 ± 0.01 | 28,157 ± 2,326 | 3.73 | 57.0 ± 7.00 | 130 ± 5 | 0.10 | 30 +3/−4 |

[a]Replicate samples from same stratigraphic horizon.

elevation of the Peninsular Ranges and FCVB depositional surface, respectively. Thus, we assign reasonable values for production rates for erosion at the sediment source, $P_E$, of 7 atoms g$^{-1}$ yr$^{-1}$ (~1000 m elevation), and for burial at the depocenter, $P_B$, of 4 atoms g$^{-1}$ yr$^{-1}$ (~300 m elevation). In section 5 we consider the scenario where the source production rate could have changed over time due to uplift.

#### 3.3.1. Sample Exhumation, $N_X$

A sample excavated from a depth $z$ beneath the outcrop surface will have an amount of $^{10}$Be produced during exhumation,

$$N_X = P_0 e^{-z\rho_s/\Lambda}\left(\frac{\Lambda}{\rho_s R_X}\right), \tag{4}$$

where $R_X$ is the local outcrop erosion rate, and $\rho_s$ is the density of the sampled sedimentary rocks, fixed here at 2.0 g/cm$^3$. The outcrop surface production rate, $P_0$, was estimated using the Lifton-Sato-Dunai nuclide-independent scaling scheme [*Lifton et al.*, 2014] as implemented in CRONUScalc version 2.0 [*Marrero et al.*, 2016], and fixed for the year 2010. Time-dependent production is not evaluated due to the uncertainty of sample exhumation rate. Sample depth, $z$, is measured from the depth of hand-augered excavations at each sample site. No additional shielding corrections were applied. The largest source of error in the $^{10}$Be contribution from sample exhumation is the local outcrop erosion rate, $R_X$. Although the late Quaternary exhumation rate of the FCVB based on its structural and stratigraphic evolution is expected to be a relatively rapid 1 to 2 mm/yr [*Dorsey et al.*, 2012], the exhumation rate at each individual outcrop could vary dramatically due to episodic erosion by landslides [*Niemi et al.*, 2005]. We account for this uncertainty for $^{10}$Be produced by spallation by placing a broad confidence limit on the local rate of erosion under which the sample was exhumed, 1.5 ± 1.0 mm/yr (2 $\sigma$), and we collected most samples from an excavated depth >60 cm to dampen the effects of shallow landsliding and reduce the overall $^{10}$Be contribution from exhumation. Deeper-penetrating muonogenic production is not strongly affected by shallow landsliding, and thus, a lower uncertainty of 0.5 mm/yr was applied to the exhumation rate for these pathways.

Error in the sample correction for exhumation, $\varepsilon_X$, relates to uncertainty in sample exhumation rate, $\delta_X$, and sample excavation depth, $\delta_z$, in a nonlinear manner,

$$\varepsilon_X = N_X\left[e^{-\frac{\rho_s\delta_z}{\Lambda}}\left(\frac{R_X}{R_X+\delta_X}\right) - 1\right]. \tag{5}$$

See Appendix A for derivation of this and subsequent error equations. Altogether, the relatively rapid uplift and erosion of the FCVB, combined with excavation of samples from below the outcrop surface, yielded $^{10}$Be concentrations that required minimal corrections for exhumation, despite the large uncertainty of outcrop erosion rate (see Table S1 in the supporting information for complete, stepwise $^{10}$Be concentration results).

#### 3.3.2. Decay, $N_D$

To derive the $^{10}$Be concentration immediately after deposition and burial of the sediment, a correction for radioactive decay over the time since deposition, $t$, is applied,

$$N_D = (N_A - N_X)(e^{\lambda t} - 1). \tag{6}$$

$\lambda$ is the decay constant, 4.997 × 10$^{-7}$ yr$^{-1}$ [*Chmeleff et al.*, 2010; *Korschinek et al.*, 2010]. Errors from decay, $\varepsilon_D$, arise from age uncertainty, $\delta_t$, due to imprecision of reversal position between paleomagnetic sample sites and due to the correlation of $^{10}$Be sample sites to the magnetostratigraphic column,

$$\varepsilon_D = (N_D + N_A - N_X)(e^{\lambda\delta_t} - 1) + \langle\varepsilon_X, \varepsilon_A\rangle(e^{\lambda(t+\delta_t)} - 1). \tag{7}$$

Note that error of the decay correction depends on the compounded error from sample exhumation, $\varepsilon_X$ and analytical error, $\varepsilon_A$ determined from measurement of $^{10}$Be.

#### 3.3.3. Burial, $N_B$

$^{10}$Be continues to be acquired by sediment after deposition, with production waning as sediment is buried. This postdepositional burial component is calculated using equation (4), substituting the burial rate, $R_B$ for $R_X$, and the thickness of paleochannel fill deposits above the sample, $y$, for the excavation depth, $z$. The burial rate is determined from the long-term sediment accumulation rate and is thus dependent on the sample site location within the FCVB, ranging from 0.6 mm/yr to 2.2 mm/yr. As in the case for deeper excavation depths, deeper paleochannels provide greater shielding of the sample, reducing the correction contributed from burial.

Errors for the burial component depend on uncertainty in the burial rate and the thickness of the sampled paleochannel fill. Paleochannel thicknesses were measured in the field with a tape measure and uncertainty, $\delta_y$, assigned from the quality of channel exposure and the thickness of the augered sample. Generally, these errors are 10 cm or less and contribute little to the overall burial error. Variation in burial rate is a potentially significant source of uncertainty, just as shallow landsliding is for the exhumation. *Balco and Stone* [2005] modeled sediment burial as an episodic process of emplacement of individual beds, drawing upon Poissonian distributions of bed thicknesses and hiatuses between sedimentation events. By sampling at the base of thick paleochannel fill deposits, we reduce the impact of such episodic sedimentation. However, intermediate-term fluctuations in sedimentation rate, perhaps due to climate cyclicity, may be expected. We thus assume a conservative uncertainty, $\delta_B$ of 50% (2 $\sigma$) for burial rate during $^{10}$Be production via spallation, and a lower, 25% uncertainty for burial rate during muonogenic $^{10}$Be production due to greater penetration depth and thus a longer averaging interval. Overall, the rapid rate of sedimentation in the FCVB, combined with collection of samples buried within thick paleochannel fill deposits, resulted in minimal corrections for sample burial.

#### 3.3.4. Paleoerosion Rate, $R_E$

To isolate the ancient $^{10}$Be concentration of the sediment at the time of erosion from the source rock, $N_E$, the concentrations accumulated during transport and burial are subtracted from the decay- and exhumation-corrected measured concentration via rearrangement of equation (3). $N_E$ is an estimate of the concentration of the ancient catchment sediment, from which a paleoerosion rate, $R_E$, may be calculated using equation (2), using an assumed production rate of $^{10}$Be during erosion in the upland sediment source region $P_E$, and the density of tonalite bedrock ($\rho = 2.7$ g/cm$^3$). Because the erosion rates in the source region are slow, we do include radioactive decay for this step. For simplicity, $^{10}$Be production is assumed to be entirely by spallation ($\Lambda = 160$ g/ cm$^2$) and we neglect the minor contribution from deeper-penetrating muons. The error in paleoerosion rate,

$$\varepsilon_E = \frac{P_E \Lambda}{\rho N_E}\left[-\frac{\langle\varepsilon\rangle}{N_E + \langle\varepsilon\rangle}\right], \tag{8}$$

where $\langle\varepsilon\rangle$ is the compounded errors from measurement, $\varepsilon_A$, exhumation, $\varepsilon_X$, radioactive decay, $\varepsilon_D$, and burial, $\varepsilon_B$.

## 4. Results

### 4.1. Paleoerosion Rates

Samples from sediment deposited in the FCVB during middle Pliocene to late Pleistocene time yield raw $^{10}$Be concentrations that range from $(5.96 \pm 0.22) \times 10^3$ to $(6.98 \pm 0.61) \times 10^4$ atoms/g (Table 3). The data show an overall decline in $^{10}$Be as the samples increase in age, consistent with loss of $^{10}$Be over time due to radioactive decay. Some samples from the northern source area with low $^{10}$Be/$^9$Be ratios exhibited large analytical uncertainties from low current yield during sample analysis. We find that samples with analytical uncertainties exceeding 30% ($2\sigma$) yield anomalously low $^{10}$Be concentrations, resulting in higher paleoerosion rates than other samples of comparable mass and age but lower analytical uncertainty.

The majority of $^{10}$Be basin samples document a consistent, stable erosion rate history (Table 4 and Figure 9). Samples from 1.0 to 3.9 Ma, excluding those with $>30\%$ analytical uncertainty, record an overall catchment-averaged, error-weighted paleoerosion rate of 38 $\pm$ 24 m/Myr (average rates reported with error-weighted $2\sigma$ confidence) (Figure 9). Paleoerosion rates derived from the southern catchment remain relatively constant between 1.9 and 3.9 Ma, ranging from between 27 and 52 m/Myr with a weighted average of 36 $\pm$ 14 m/Myr (Figure 9). At three horizons, two or three samples were collected along strike to test the reproducibility of results. At each location, the paleoerosion rates agree within error (Table 4). Erosion rates for northern catchment-derived sediment, excluding results with >30% analytical uncertainty, ranged between 20 and 110 mm/yr, with a weighted average of 41 $\pm$ 37 m/Myr (Figure 9), which agrees with the southern catchment samples. Excess scatter for the northern source samples may be attributed to higher analytical uncertainties, as well as to shallower excavation depths for many samples (Table 4).

### 4.2. Modern Catchment-Averaged Erosion Rates

Sediment samples collected from modern streambeds were also analyzed using cosmogenic $^{10}$Be. Raw $^{10}$Be concentrations range from $(8.1 \pm 2.0) \times 10^4$ to $(1.5 \pm 0.1) \times 10^5$ atoms/g (Table 3), significantly higher than the basin sediment concentrations. Catchment erosion rates were calculated using a $^{10}$Be production rate of 7 atoms/g/yr, in order to compare these directly with paleoerosion rates calculated with this production

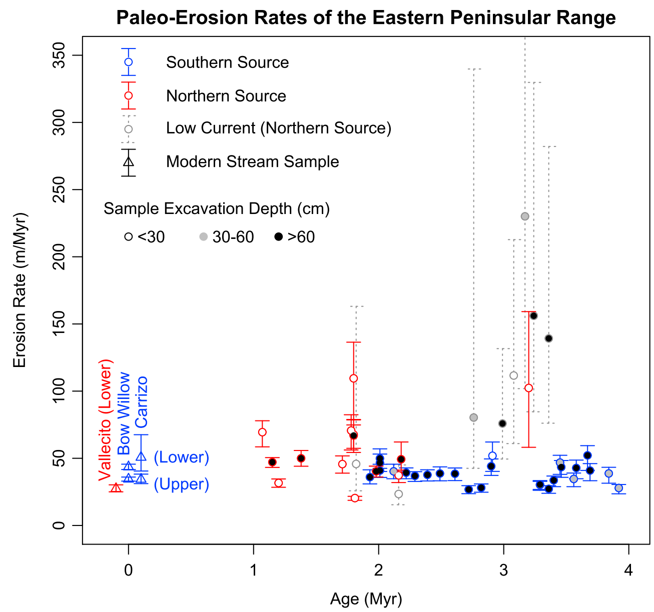


**Figure 9.** Paleoerosion rates for the eastern Peninsular Range derived from $^{10}$Be concentrations in sediment from the FCVB. Northern and southern sediment sources (see Figure 3) exhibit uniform, slow rates of catchment-averaged erosion from 4 Ma to present. Low current samples with >30% analytical uncertainty yield anomalously low $^{10}$Be concentration, resulting in higher paleoerosion rates with large errors. Error bars represent 95% confidence derived from 100,000 random variations of input parameters for each sample.

rate (Figure 9 and Table 4). The erosion rates thus calculated vary between 27 and 51 m/Myr, consistent with paleoerosion rates from both the northern and southern source regions. Samples collected from the lower Carrizo Gorge and Bow Willow wash each exhibit slightly higher erosion rates (51 and 44 m/Myr) than samples collected where these same two washes exit the plateau (both 34 m/Myr). This is consistent with dilution by sediment input from the more rapidly eroding escarpment region.

## 5. Discussion

Analysis of $^{10}$Be in sediments collected from the FCVB indicates that catchment-averaged paleoerosion rates in the upland sediment source have remained largely unchanged from 4 Ma to 1 Ma, a period that encompasses the onset of Northern Hemisphere glaciation and increased global climate variability after ~3 Ma [e.g., *Raymo et al.*, 1989; *Raymo*, 1994], as well as locally cooling sea surface temperature and increased aridity [*Ravelo et al.*, 2004; *Peryam et al.*, 2011]. The constant erosion rate implies that progradation of locally derived sediment into the FCVB was probably a response to slowing of basin subsidence rates and does not reflect a sustained increase in sediment input flux.

At an average erosion rate of 40 m/Myr, the recovery time scale for a pulse of erosion would be 15 kyr, which is too short to be clearly resolved within the resolution of our paleoerosion rate record. Sustained enhanced erosion rate, over multiple climate change cycles, would need to have occurred to be confidently recorded by our $^{10}$Be data. The gradual increase in aridity from the late Pliocene to the Pleistocene [*Peryam et al.*, 2011] should have led to decreased vegetation cover and that could have, in turn, led to a period of enhanced erosion due to repeated vegetation shifts with climate changes [*Pelletier*, 2014]. Some of the scatter in the paleoerosion rate results (Figure 9) may indeed record periodic vegetation change-induced erosion pulses (e.g., the decline in erosion rate from 50 m/Myr to 30 m/Myr in the southern source from 2.9 to 2.7 Ma). However, this variation is no larger than the scatter in results from 4 Ma to 3 Ma, prior to the cooling in sea surface temperature offshore Southern California [*Ravelo et al.*, 2004]. Overall, the paleoerosion rate record from the southern catchment, and most of the data from the northern catchment, supports that erosion rates have remained constant and little affected by changes in climate that have occurred since the middle Pliocene, with the caveat that short pulses of enhanced erosion, over a limited depth, cannot be resolved with $^{10}$Be.

Modern catchment-averaged erosion rates are similar to paleoerosion rates from 1.0 to 3.9 Ma. Due to the shift from basin subsidence to uplift after ~1.2 Ma, no basin sediment younger than ~1.0 Ma was collected, and therefore no erosion rates between 1.0 Ma and present were derived. The consistency of modern and ancient erosion rates suggests that the 1.2 Ma tectonic reorganization of the FCVB has not yet measurably impacted the average rate of erosion in the Peninsular Ranges. Conceivably, short-term climatically driven fluctuations in the paleoerosion rate could have occurred between 1.0 Ma and present but were not recorded.

The similarity in both modern and paleoerosion rates for the northern and southern source regions is somewhat surprising given their different present-day topography. While the southern catchment is dominated by gently sloped uplands, the majority of erosion in the northern catchment probably occurred along a steep escarpment, similar to today. It is unlikely that the physiographic characteristics of these landscapes have changed significantly over the past 2 Myr, given the very low rates of erosion overall. Perhaps the erosion rates are insensitive to the differences between the catchments. Alternatively, a slower rate of sediment transport out of the northern catchment may counterbalance a higher erosion rate in the sediment source region. Temporary sediment storage on desert pediments has been shown to measurably contribute to surface-exposure ages [*Nichols et al.*, 2007]. If this is the case for the lowland piedmont of the Vallecito catchment, it would violate the instantaneous transport assumed when correcting $^{10}$Be concentrations ($N_T \approx 0$). The additional $^{10}$Be acquired during transport would result in an effective erosion rate measured where the sediment enters the FCVB that was slower than the actual erosion rate of the escarpment. Additional measurements of catchment-averaged erosion rates closer to the sediment source region are needed to test these competing hypotheses.

In this study it is assumed that little change in elevation of the source region has occurred over the past 4 Myr, which is supported by evidence of a rain shadow in place by 3.8 Ma [*Peryam et al.*, 2011]. If elevation change did occur, it would affect the $^{10}Be$ production rate over time and thus impact paleoerosion rates. Surface lowering by erosion is not enough to substantively change the elevation; integrated over the past 4 Myr, it accounts for 200 m of exhumation, most of which would be accommodated by isostatically driven rock uplift rather than surface lowering. Even without isostatic recovery, this change in elevation has only a modest effect on $^{10}Be$ production rate (~1 atom/g/yr). A more substantial potential elevation change is surface uplift of the Peninsular Ranges as a tilted normal-fault footwall and rift flank, as has been suggested from studies of Plio-Pleistocene marine terraces on the Pacific coast [*Mueller et al.*, 2009]. If uplifted from near sea level to its current elevation over the past 4 Myr, the $^{10}Be$ production rate would have increased with the elevation, from 4 at/g/yr to 7 at/g/yr. Reevaluating our paleoerosion rates with such a history of footwall uplift would result in paleoerosion rates steadily increasing by almost a factor of 2 between 4 Ma and present for samples with the same concentration of $^{10}Be$. Such a steady temporal increase in paleoerosion rate would be consistent with an increase in tectonic forcing. Though this scenario cannot be completely ruled out, it is inconsistent with the presence of a rain shadow, and with coarse footwall-derived Plio-Pleistocene detritus preserved adjacent to the West Salton Detachment fault and interfingering with the entire sedimentary section analyzed in this study [*Dorsey et al.*, 2012].

In summary, sediments of the FCVB do not record an increase in paleoerosion rate in response to climate change approximately 3 Ma. The observed progradation of locally sourced sediment into the FCVB approximately 2.8 – 2.9 Ma immediately follows a marked decrease in basin subsidence rate [*Dorsey et al.*, 2011] and reflects the expected adjustment of coarse sediment deposition to this rate decrease [*Paola et al.*, 1992].

## 6. Conclusion

$^{10}$Be analysis from the FCVB provides a robust temporal erosion rate record from 4 Ma to 1 Ma. The erosion rates do not show an expected increase in response to a global increase in climate variation approximately 3 Ma and locally enhanced aridity. Paleoerosion rates that produced sediment transported to the FCVB remained consistent, at ~40 m/Myr, between 1 and 4 Ma, and are similar to modern catchment-averaged erosion rates. In the FCVB, a change in basin subsidence rate, without a change in paleoerosion rate, drove abrupt progradation of locally sourced alluvial fans.

The time series of catchment-averaged erosion rates reported here was derived from sediment collected in one basin. While the erosion rates, derived from a dense array of samples, are very consistent over time, the FCVB is but one of a few examples worldwide where such a long and detailed record has been obtained [*Granger and Schaller*, 2014]. Other landscapes, especially in more humid settings [*Refsnider*, 2010], or where subjected to glacial erosion [*Charreau et al.*, 2011], may have responded quite differently to the approximately 3 Ma climate shift. Deducing the linkages between erosion, climate, and tectonics with cosmogenic nuclide archives requires careful attention to the range of posterosion processes and uncertainties that affect nuclide concentrations [*Val et al.*, 2016]. Further paleoerosion rate studies are needed to test the response of other landscapes, both glaciated and unglaciated, to changes in climate forcing over the late Cenozoic. The FCVB example demonstrates that high-precision, reproducible paleoerosion rate measurements can be obtained from sedimentary basins with well-constrained source regions, precise age control, a high ratio of subsidence rate to erosion rate, and well-constrained sediment exposure history.

## Appendix A: Paleoerosion Rate Error Analysis

Uncertainties are assessed retroactively over the lifetime of the sample, beginning with exhumation of the sediment, followed by decay, burial, and finally, the erosion in the source region. No uncertainty is assessed for the fluvial transport component, which we assume to be negligible. Due to the exponential processes controlling $^{10}$Be ingrowth and decay, each level of uncertainty depends on error components that were assessed at previous steps. To fully capture these dependencies, uncertainties are summed using a Monte Carlo approach to select values randomly from each parameter with its own range and normally distributed uncertainty and iterated over each of the three production pathways for $^{10}$Be. This appendix describes the equations and parameters used at each level of the uncertainty calculation. Each component of error is represented by an addition of a variable, $\varepsilon$, which is then isolated.

### A1. Sample Exhumation Error, $\varepsilon_X$

We begin with an equation for ingrowth of $^{10}$Be during sample exhumation, $N_X$, including an error component, $\varepsilon_X$. The error depends both on uncertainty of sample depth, $z + \delta_z$ and erosion rate of the sedimentary rocks at the sample site, $R_x + \delta_X$.

$$N_X + \varepsilon_X = P_0 e^{-\frac{\rho_S(z+\delta_Z)}{\Lambda}} \left( \frac{\Lambda}{\rho_S(R_x + \delta_x)} \right). \tag{A1}$$

Subtracting the equation for $N_X$ (equation (4)) yields

$$\varepsilon_X = P_0 e^{-\frac{\rho_S(z+\delta_Z)}{\Lambda}} \left( \frac{\Lambda}{\rho_S(R_x + \delta_x)} \right) - P_0 e^{-\frac{\rho_S z}{\Lambda}} \frac{\Lambda}{\rho_s R_X}. \tag{A2}$$

This may be simplified to show that the error is proportional as well to $N_X$,

$$\varepsilon_X = P_0 \frac{\Lambda}{\rho_s R_X} e^{-\frac{\rho_S z}{\Lambda}} \left[ e^{-\frac{\rho_S \delta_Z}{\Lambda}} \left( \frac{R_X}{R_X + \delta_X} \right) - 1 \right], \tag{A3}$$

$$\varepsilon_X = N_X \left[ e^{-\frac{\rho_S \delta_Z}{\Lambda}} \left( \frac{R_X}{R_X + \delta_X} \right) - 1 \right]. \tag{A4}$$

### A2. Radioactive Decay Error, $\varepsilon_D$

Error for the decay correction proceeds in a similar manner, by adding and then isolating the error component, $\varepsilon_D$,

$$N_D + \varepsilon_D = (N_A - N_X + \langle \varepsilon_X, \varepsilon_A \rangle)(e^{\lambda(t+\delta_t)} - 1). \tag{A5}$$

Recall that $\langle \varepsilon_X, \varepsilon_A \rangle$ is the compounded analytical uncertainty and error in concentration from correction for sample exhumation. Next, subtract the equation for $N_D$ (equation (6)),

$$\varepsilon_D = (N_A - N_X + \langle \varepsilon_X, \varepsilon_A \rangle)(e^{\lambda(t+\delta_t)} - 1) - (N_A - N_X)(e^{\lambda t} - 1), \tag{A6}$$

then simplify and substitute $N_D$,

$$\varepsilon_D = (N_A - N_X) e^{\lambda t}(e^{\lambda \delta_t} - 1) + \langle \varepsilon_X, \varepsilon_A \rangle (e^{\lambda(t+\delta_t)} - 1). \tag{A7}$$

$$\varepsilon_D = (N_D + N_A - N_X)(e^{\lambda \delta_t} - 1) + \langle \varepsilon_X, \varepsilon_A \rangle (e^{\lambda(t+\delta_t)} - 1). \tag{A8}$$

### A3. Burial Error, $\varepsilon_B$

Error for $^{10}$Be acquired during sediment burial in the basin follows the same procedure as equations (A1)–(A4), with the result,

$$\varepsilon_B = N_B \left[ e^{-\frac{\rho_S \delta y}{\Lambda}} \left( \frac{R_B}{R_B + \delta_B} \right) - 1 \right]. \tag{A9}$$

### A4. Paleoerosion Rate Error, $\varepsilon_E$

Paleoerosion rate error depends on the compounded errors, $\langle \varepsilon \rangle$ from sample exhumation, radioactive decay, and burial. Proceeding in a similar manner,

$$R_E + \varepsilon_E = \frac{\Lambda}{\rho} \left( \frac{P_E}{N_E + \langle \varepsilon \rangle} - \lambda \right). \tag{A10}$$

Subtract the equation for erosion rate, $R_E$ (equation (2), using the assumed production rate at the sediment source, $P_E$, and simplify

$$\varepsilon_E = \frac{\Lambda}{\rho} \left( \frac{P_E}{N_E + \langle \varepsilon \rangle} - \lambda \right) - \frac{\Lambda}{\rho} \left( \frac{P_E}{N_E} - \lambda \right). \tag{A11}$$

$$\varepsilon_E = \frac{P_E \Lambda}{\rho} \left( \frac{1}{N_E + \langle \varepsilon \rangle} - \frac{1}{N_E} \right) \tag{A12}$$

$$\varepsilon_E = -\frac{P_E \Lambda}{\rho N_E} \left( \frac{\langle \varepsilon \rangle}{N_E + \langle \varepsilon \rangle} \right) \tag{A13}$$

The negative sign arises because a positive error in concentration will reduce the value of erosion rate. For the case where the impact of radioactive decay during erosion can be neglected, equation (A13) simplifies

$$\varepsilon_E \approx -R_E \left( \frac{\langle \varepsilon \rangle}{N_E + \langle \varepsilon \rangle} \right). \tag{A14}$$

**Acknowledgments**
All supporting data are included in this contribution and in the supporting information. This research was supported by the U.S. National Science Foundation, Tectonics program, and Geomorphology and Land Use Dynamics program, award EAR-0739017 and EAR-0838151 to Oskin, EAR-0711222 and EAR-0838119 to Dorsey, and EAR-0710988 and EAR-0838167 to Housen. We thank the Anza-Borrego Desert State Park for permission to sample to the Fish Creek-Vallecito badlands. We appreciate the constructive feedback from Editor J. Buffington, Associate Editor J. Pelletier, and reviewer A. Darling and an anonymous reviewer.

## References

Axen, G., and J. Fletcher (1998), Late Miocene-Pleistocene extensional faulting, northern Gulf of California, Mexico and Salton Trough, California, *Int. Geol. Rev.*, *40*, 217–244.

Balco, G., and J. Stone (2005), Measuring middle Pleistocene erosion rates with cosmic-ray-produced nuclides in buried alluvial sediment, Fisher Valley, southeastern Utah, *Earth Surf. Processes Landforms*, *30*, 1051–1067, doi:10.1002/esp.1262.

Braucher, R., E. Brown, D. Bourlès, and F. Colin (2003), In situ produced $^{10}$Be measurements at great depths: Implications for production rates by fast muons, *Earth Planet. Sci. Lett.*, *211*(3-4), 251–258, doi:10.1016/S0012-821X(03)00205-X.

Brierley, C. M., A. V. Fedorov, Z. Liu, T. D. Herbert, K. T. Lawrence, and J. P. LaRiviere (2009), Greatly expanded tropical warm pool and weakened Hadley circulation in the Early Pliocene, *Science*, *323*(5922), 1714–1718.

Brown, E., D. L. Bourles, F. Colin, G. M. Raisbeck, F. Yiou, and S. Desgarceaux (1995), Evidence for muon-induced production of $^{10}$Be in near-surface rocks from the Congo, *Geoph. Res. Lett.*, *22*(6), 703–706.

Brown, E. T., R. F. Stallard, M. C. Larsen, D. L. Bourlès, G. M. Raisbeck, and F. Yiou (1998), Determination of predevelopment denudation rates of an agricultural watershed (Cayaguas River, Puerto Rico) using in-situ-produced $^{10}$Be in river-borne quartz, *Earth Planet. Sci. Lett.*, *160*(3), 723–728.

Bull, W. L. (1991), *Geomorphic Responses to Climatic Change*, Oxford Univ. Press, New York.

Cerling, T. E., and H. Craig (1994), Geomorphology and in-situ cosmogenic isotopes, *Annu. Rev. Earth Planet. Sci.*, *22*, 273–317.

Charreau, J., et al. (2011), Paleo-erosion rates in Central Asia since 9 Ma: A transient increase at the onset of Quaternary glaciations?, *Earth Planet. Sci. Lett.*, *304*(1–2), 85–92, doi:10.1016/j.epsl.2011.01.018.

Chmeleff, J., F. von Blanckenburg, K. Kossert, and D. Jakob (2010), Determination of the 10be half-life by multicollector ICP-MS and liquid scintillation counting, *Nucl. Instrum. Methods Phys. Res.*, *268*(2), 192–199, doi:10.1016/j.nimb.2009.09.012.

Clemens, S. C., and R. Tiedemann (1997), Eccentricity forcing of Pliocene-Early Pleistocene climate revealed in a oxygen-isotope record, *Nature*, *385*(801–804).

Dekens, P. S., A. C. Ravelo, and M. D. McCarthy (2007), Warm upwelling regions in the Pliocene warm period, *Paleoceanography*, *22*(3), PA3211, doi:10.1029/2006PA001394.

Desilets, D., and M. Zreda (2003), Spatial and temporal distribution of secondary cosmic-ray nucleon intensities and applications to in situ cosmogenic dating, *Earth Planet. Sci. Lett.*, *206*(1), 21–42.

Desilets, D., M. Zreda, and T. Prabu (2006), Extended scaling factors for in situ cosmogenic nuclides: New measurements at low latitude, *Earth Planet. Sci. Lett.*, *246*(3–4), 265–276, doi:10.1016/j.epsl.2006.03.051.

Dibblee, T. (1954), Geology of the Imperial Valley region, California, in *Geology of Southern California*, vol. 170, edited by R. Jahns, pp. 21–28, California Division of Mines, Sacramento, Calif.

Dibblee, T. (1984), *Stratigraphy and Tectonics of the San Felipe Hills, Borrego Badlands, Superstition Hills, and Vicinity*.

Dibblee, T. (1996), Stratigraphy and tectonics of the Vallecito-Fish Creek Mountains, Vallecito Badlands, Coyote Mountains, and Yuha Desert, southwestern Imperial Basin, in *Sturzstroms and Detachment Faults, Anza-Borrego Desert State Park, California*, vol. 24, edited by L. Abbott and D. Seymour, pp. 59–80, South Coast Geological Society, Santa Ana, Calif.

Dorsey, R. (2006), Stratigraphy, tectonics, and basin evolution in the Anza-Borrego Desert region, in *Fossil Treasures of the Anza-Borrego Desert*, edited by G. T. Jefferson and L. Lindsay, pp. 89–104, Sunbelt Publ., San Diego, Calif.

Dorsey, R. J., A. Fluette, K. McDougall, B. A. Housen, S. U. Janecke, G. J. Axen, and C. R. Shirvell (2007), Chronology of Miocene-Pliocene deposits at Split Mountain Gorge, Southern California: A record of regional tectonics and Colorado River evolution, *Geology*, *35*, 57–60, doi:10.1130/G23139A.1.

Dorsey, R. J., B. A. Housen, S. U. Janecke, C. M. Fanning, and A. L. F. Spears (2011), Stratigraphic record of basin development within the San Andreas fault system: Late Cenozoic Fish Creek-Vallecito basin, southern California, *Geol. Soc. Am. Bul.*, *123*(5–6), 771–793, doi:10.1130/B30168.1.

Dorsey, R. J., G. J. Axen, T. C. Peryam, and M. E. Kairouz (2012), Initiation of the southern Elsinore fault at ∼1.2 Ma: Evidence from the Fish Creek-Vallecito Basin, Southern California, *Tectonics*, *31*(2), TC2006, doi:10.1029/2011TC003009.

Dosseto, A., and M. Schaller (2016), The erosion response to Quaternary climate change quantified using uranium isotopes and in situ-produced cosmogenic nuclides, *Earth Sci. Rev.*, *155*, 60–81, doi:10.1016/j.earscirev.2016.01.015.

Dunai, T. J. (2000), Scaling factors for production rates of in situ produced cosmogenic nuclides: A critical reevaluation, *Earth Planet. Sci. Lett.*, *176*, 157–169.

Dunai, T. J. (2001), Influence of secular variation of the geomagnetic field on production rates of in situ produced cosmogenic nuclides, *Earth Planet. Sci. Lett.*, *193*(1–2), 197–212.

Fedorov, A. V., C. M. Brierley, K. T. Lawrence, Z. Liu, P. S. Dekens, and A. C. Ravelo (2013), Patterns and mechanisms of early Pliocene warmth, *Nature*, *496*(7443), 43–49, doi:10.1038/nature12003.

Finnegan, N. J., B. Hallet, D. R. Montgomery, P. K. Zeitler, J. O. Stone, A. M. Anders, and L. Yuping (2008), Coupling of rock uplift and river incision in the Namche Barwa-Gyala Peri massif, Tibet, *Geol. Soc. Am. Bull.*, *120*(1–2), 142–155, doi:10.1130/1326224.1.

Godard, V., G. E. Tucker, G. Burch Fisher, D. W. Burbank, and B. Bookhagen (2013), Frequency-dependent landscape response to climatic forcing, *Geophys. Res. Lett.*, *40*(5), 859–863, doi:10.1002/grl.50253.

Gradstein, F. (2013), *The Geologic Time Scale 2012*, Elsevier, San Francisco, Calif.

Granger, D., J. Kirchner, and R. Finkel (1996), Spatially averaged long-term erosion rates measured from in situ-produced cosmogenic nuclides in alluvial sediment, *J. Geol.*, *104*(3), 249–257.

Granger, D., J. Kirchner, and R. Finkel (1997), Quaternary downcutting rate of the New River, Virginia, measured from differential decay of cosmogenic Al-26 and Be-10 in cave-deposited alluvium, *Geology*, *25*, 107–110.

Granger, D., D. Fabel, and A. Palmer (2001), Pliocene-Pleistocene incision of the Green River, Kentucky, determined from radioactive decay of cosmogenic Al-26 and Be-10 in Mammoth Cave sediments, *Geol. Soc. Am. Bull.*, *113*(7), 825–836.

Granger, D. E. (2006), A review of burial dating methods using $^{26}$Al and $^{10}$Be, in *Special Paper 415: In Situ-Produced Cosmogenic Nuclides and Quantification of Geological Processes*, vol. 415, pp. 1–16, Geological Society of America, Boulder, Colo.

Granger, D. E., and M. Schaller (2014), Cosmogenic nuclides and erosion at the watershed scale, *Elements*, *10*(5), 369–373, doi:10.2113/gselements.10.5.369.

Haug, G. H., et al. (2005), North Pacific seasonality and the glaciation of North America 2.7 million years ago, *Nature*, *433*(7028), 821–825.

Hay, W. W., J. L. Sloan, and C. N. Wold (1988), Mass/age distribution and composition of sediments on the ocean floor and the global rate of sediment subduction, *J. Geophys. Res.*, *93*(B12), 14,933–14,940.

Heisinger, B., D. Lal, A. J. T. Jull, P. Kubik, S. Ivy-Ochs, S. Neumaier, K. Knie, V. Lazarev, and E. Nolte (2002a), Production of selected cosmogenic radionuclides by muons: 1. Fast muons, *Earth Planet. Sci. Lett.*, *200*(3), 345–355.

Heisinger, B., D. Lal, A. J. T. Jull, P. W. Kubik, S. Ivy-Ochs, K. Knie, and E. Nolte (2002b), Production of selected cosmogenic radionuclides by muons: 2. Capture of negative muons, *Earth Planet. Sci. Lett.*, *200*, 357–369.

Herman, F., D. Seward, P. G. Valla, A. Carter, B. Kohn, S. D. Willett, and T. A. Ehlers (2013), Worldwide acceleration of mountain erosion under a cooling climate, *Nature*, *504*(7480), 423–426, doi:10.1038/nature12877.

Janecke, S. U., R. J. Dorsey, D. Forand, A. N. Steely, S. Kirby, A. T. Lutz, B. A. Housen, B. Belgarde, V. E. Langenheim, and T. M. Rittenhour (2010), *High Geologic Slip Rates since Early Pleistocene Initiation of the San Jacinto and San Felipe Fault Zones in the San Andreas Fault System: Southern California, USA, Geol. Soc. Am. Spec. Pap.*, vol. 475, Geological Society of America, Boulder, Colo.

Johnson, N., C. Officer, N. Opdyke, G. Woodard, P. Zeitler, and E. Lindsay (1983), Rates of Late Cenozoic tectonism in the Vallecito-Fish Creek Basin, western Imperial Valley, California, *Geology*, *11*, 664–667.

Keeler-Wolf, T., K. Lewis, and C. Roye, (1998), Vegetation Mapping of Anza-Borrego Desert State Park and Environs, Tech. Rep. C433000, California Department of Fish and Game, Sacramento, Calif.

Kerr, D. (1984), Early Neogene continental sedimentation in the Vallecito and Fish Creek mountains, western Salton Trough, California, *Sediment. Geol.*, *38*, 217–246.

Kerr, D., S. Kidwell, M. Walawender, and B. Hanan (1991), Late Cenozoic sedimentation and tectonics, western Salton Trough, California, in *Geological Excursions in Southern California and Mexico*, pp. 397–416, San Diego State Univ., San Diego, Calif.

Kirby, S. M., S. U. Janecke, R. J. Dorsey, B. A. Housen, V. E. Langenheim, K. A. McDougall, and A. N. Steely (2007), Pleistocene Brawley and Ocotillo formations: Evidence for initial strike-slip deformation along the San Felipe and San Jacinto fault zones, southern California, *J. Geol.*, *115*(1), 42–62.

Korschinek, G., et al. (2010), A new value for the half-life of $^{10}$Be by Heavy-Ion Elastic Recoil Detection and liquid scintillation counting, *Nucl. Instrum. Methods Phys. Res.*, *268*(2), 187–191, doi:10.1016/j.nimb.2009.09.020.

Lal, D. (1991), Cosmic-ray labeling of erosion surfaces—In situ nuclide production-rates and erosion models, *Earth Planet. Sci. Lett.*, *104*(2–4), 424–439.

Lifton, N., T. Sato, and T. J. Dunai (2014), Scaling in situ cosmogenic nuclide production rates using analytical approximations to atmospheric cosmic-ray fluxes, *Earth Planet. Sci. Lett.*, *386*, 149–160, doi:10.1016/j.epsl.2013.10.052.

Longinotti, N. E. (2012), *$^{10}$Be-Derived Paleo-Erosion Rates Recorded in the Fish Creek-Vallecito Basin, California Since 4 Ma Indicate No Increase Across the Plio-Pleistocene Climate Transition, M.S.*, Univ. of California, Davis, Calif.

Lutz, A. T., R. J. Dorsey, B. A. Housen, and S. U. Janecke (2006), Stratigraphic record of Pleistocene faulting and basin evolution in the Borrego Badlands, San Jacinto fault zone, Southern California, *Geol. Soc. Am. Bull.*, *118*, 1377–1397, doi:10.1130/B25946.1.

Marrero, S. M., F. M. Phillips, B. Borchers, N. Lifton, R. Aumer, and G. Balco (2016), Cosmogenic nuclide systematics and the CRONUScalc program, *Quat. Geochronol.*, *31*, 160–187, doi:10.1016/j.quageo.2015.09.005.

Minch, J. (1979), The Late Mesozoic-Early Tertiary framework of continental sedimentation, northern Peninsular Ranges, Baja California, Mexico, in *Eocene Depositional Systems*, edited by P. L. Abbott, pp. 43–67, Society of Economic Paleontologists and Mineralogists, San Diego, Calif.

Molnar, P. (2004), Late Cenozoic increase in accumulation rates of terrestrial sediment: How might climate change have affected erosion rates?, *Annu. Rev. Earth Sci.*, *32*, 67–89, doi:10.1146/annurev.earth.32.091003.143456.

Molnar, P., and P. England (1990), Late Cenozoic uplift of mountain-ranges and global climate change: Chicken or egg?, *Nature*, *346*, 29–34.

Mueller, K., G. Kier, T. Rockwell, and C. H. Jones (2009), Quaternary rift flank uplift of the Peninsular Ranges in Baja and southern California by removal of mantle lithosphere, *Tectonics*, *28*(5), doi:10.1029/2007TC002227.

Nichols, K. K., P. R. Bierman, M. C. Eppes, M. Caffee, R. Finkel, and J. Larsen (2007), Timing of surficial process changes down a Mojave Desert piedmont, *Quat. Res.*, *68*, 151–161, doi:10.1016/j.yqres.2007.02.001.

Niemi, N. A., M. E. Oskin, D. W. Burbank, A. M. Heimsath, and E. J. Gabet (2005), Effects of bedrock landslides on cosmogenically determined erosion rates, *Earth Planet. Sci. Lett.*, *237*, 480–498.

Nishiizumi, K., M. Imamura, M. W. Caffee, J. R. Southon, R. C. Finkel, and J. McAninch (2007), Absolute calibration of $^{10}$Be AMS standards, *Nucl. Instrum. Methods Phys. Res.*, *258*(2), 403–413, doi:10.1016/j.nimb.2007.01.297.

Opdyke, N., E. Lindsay, N. Johnson, and T. Downs (1977), The paleomagnetism and magnetic polarity stratigraphy of the mammal-bearing section of Anza-Borrego State Park, California, *Quat. Res.*, *7*, 316–329.

Paola, C., P. L. Heller, and C. L. Angevine (1992), The large-scale dynamics of grain-size variation in alluvial basins, 1: Theory, *Basin Res.*, *4*(2), 73–90.

Pelletier, J. D. (2014), The linkages among hillslope-vegetation changes, elevation, and the timing of late-Quaternary fluvial-system aggradation in the Mojave Desert revisited, *Earth Surf. Dyn.*, *2*(2), 455–468, doi:10.5194/esurf-2-455-2014.

Pelletier, J. D., M. H. Nichols, and M. A. Nearing (2016), The influence of Holocene vegetation changes on topography and erosion rates: A case study at Walnut Gulch Experimental Watershed, Arizona, *Earth Surf. Dyn.*, *4*(2), 471–488, doi:10.5194/esurf-4-471-2016.

Peryam, T. C., R. J. Dorsey, and I. Bindeman (2011), Plio-Pleistocene climate change and timing of Peninsular Ranges uplift in southern California: Evidence from paleosols and stable isotopes in the Fish Creek-Vallecito basin, *Palaeogeogr. Palaeoclimatol. Palaeoecol.*, *305*(1–4), 65–74, doi:10.1016/j.palaeo.2011.02.014.

Puchol, N., J. Charreau, P.-H. Blard, J. Lave, S. Dominguez, R. Pik, D. Saint-Carlier, and ASTER Team (2017), Limited impact of Quaternary glaciations on denudation rates in Central Asia, *Geol. Soc. Am. Bull.*, *129*(3/4), 479–499, doi:10.1130/B31475.1.

Ravelo, A. C., D. H. Andreasen, M. Lyle, A. O. Lyle, and M. W. Wara (2004), Regional climate shifts caused by gradual global cooling in the Pliocene epoch, *Nature*, *429*(6989), 263–267.

Raymo, M., and W. Ruddiman (1992), Tectonic forcing of Late Cenozoic climate, *Nature*, *359*, 117–122.

Raymo, M. E. (1994), The initiation of Northern Hemisphere glaciation, *Annu. Rev. Earth Planet. Sci.*, *22*, 353–383.

Raymo, M. E., W. Ruddiman, J. Backman, B. Clement, and D. Martinson (1989), Late Pliocene variation in Northern Hemisphere ice sheets and North Atlantic deep water circulation, *Paleoceanography*, *4*(4), 413–446.

Refsnider, K. A. (2010), Dramatic increase in late Cenozoic alpine erosion rates recorded by cave sediment in the southern Rocky Mountains, *Earth Planet. Sci. Lett.*, *297*(3–4), 505–511, doi:10.1016/j.epsl.2010.07.002.

Riebe, C., J. Kirchner, D. Granger, and R. Finkel (2001), Strong tectonic and weak climatic control of long-term chemical weathering rates, *Geology*, *29*, 511–514.

Sadler, P. (1981), Sediment accumulation rates and the completeness of stratigraphic sections, *J. Geol.*, *89*, 569–584.

Sadler, P. M., and D. J. Jerolmack (2015), Scaling laws for aggradation, denudation and progradation rates: The case for time-scale invariance at sediment sources and sinks, *Geol. Soc. London, Spec. Pub.*, *404*(1), 69–88, doi:10.1144/SP404.7.

Schaller, M., and T. A. Ehlers (2006), Limits to quantifying climate driven changes in denudation rates with cosmogenic radionuclides, *Earth Planet. Sci. Lett.*, *248*, 153–167, doi:10.1016/j.epsl.2006.05.027.

Schaller, M., F. Von Blanckenburg, A. Veldkamp, L. A. Tebbens, N. Hovius, and P. W. Kubik (2002), A 30,000 yr record of erosion rates from cosmogenic $^{10}$Be in Middle European river terraces, *Earth Planet. Sci. Lett.*, *204*(1), 307–320.

Schaller, M., F. Von Blanckenburg, N. Hovius, A. Veldkamp, M. W. van den Berg, and P. W. Kubik (2004), Paleoerosion rates from cosmogenic $^{10}$Be in a 1.3 Ma terrace sequence: Response of the River Meuse to changes in climate and rock uplift, *J. Geol.*, *112*(2), 127–144.

Shirvell, C. R., D. F. Stockli, G. J. Axen, and M. Grove (2009), Miocene-Pliocene exhumation along the west Salton detachment fault, southern California, from (U-Th)/He thermochronometry of apatite and zircon, *Tectonics*, *28*(2), TC2006, doi:10.1029/2007TC002172.

Steely, A. N., S. U. Janecke, R. J. Dorsey, and G. J. Axen (2009), Early Pleistocene initiation of the San Felipe fault zone, SW Salton Trough, during reorganization of the San Andreas fault system, *Geol. Soc. Am. Bull.*, *121*(5–6), 663–687, doi:10.1130/B26239.1.

Stock, G., R. Anderson, and R. Finkel (2004), Pace of landscape evolution in the Sierra Nevada, California, revealed by cosmogenic dating of cave sediments, *Geology*, *32*(3), 193–196, doi:10.1130/G20197.1.

Stone, J. (2000), Air pressure and cosmogenic isotope production, *J. Geophys. Res.*, *105*, 23,753–23,759.

Todd, V., (2004), Preliminary geologic map of the El Cajon $30' \times 60'$ Quadrangle, Southern California, *U.S. Geol. Surv. Open File Rep., 2004-1361*.

Val, P., G. D. Hoke, J. C. Fosdick, and H. Wittmann (2016), Reconciling tectonic shortening, sedimentation and spatial patterns of erosion from $^{10}$Be paleo-erosion rates in the Argentine Precordillera, *Earth Planet. Sci. Lett.*, *450*, 173–185, doi:10.1016/j.epsl.2016.06.015.

Valet, J., L. Meynadier, and Y. Guyodo (2005), Geomagnetic dipole strength and reversal rate over the past two million years, *Nature*, *435*(7043), 802–805, doi:10.1038/nature03674.

West, A. J., R. Hetzel, G. Li, Z. Jin, F. Zhang, R. G. Hilton, and A. L. Densmore (2014), Dilution of $^{10}$Be in detrital quartz by earthquake-induced landslides: Implications for determining denudation rates and potential to provide insights into landslide sediment dynamics, *Earth Planet. Sci. Lett.*, *396*, 143–153, doi:10.1016/j.epsl.2014.03.058.

Whipple, K. X., and G. E. Tucker (1999), Dynamics of the stream-power river incision model: Implications for height limits of mountain ranges, landscape response timescales, and research needs, *J. Geophys. Res.*, *104*(B8), 17,661–17,674, doi:10.1029/1999JB900120.

Willenbring, J. K., and F. von Blanckenburg (2010), Meteoric cosmogenic Beryllium-10 adsorbed to river sediment and soil: Applications for Earth-surface dynamics, *Earth Sci. Rev.*, *98*(1–2), 105–122, doi:10.1016/j.earscirev.2009.10.008.

Willett, S. D. (1999), Orogeny and orography: The effects of erosion on the structure of mountain belts, *J. Geophys. Res.*, *104*(B12), 28,957–28,981.

Winker, C. (1987), Neogene stratigraphy of the Fish Creek-Vallecito section, Southern California: Implications for Early History of the Northern Gulf of California and the Colorado Delta, PhD thesis, Univ. of Arizona, Tucson, Ariz.

Winker, C., and S. Kidwell (1996), Stratigraphy of a marine rift basin: Neogene of the western Salton Trough, California, in *Field Conference Guidebook and Volume for the American Association of Petroleum Geologists Annual Convention*, edited by P. L. Abbott and J. Cooper, pp. 295–336, American Association of Petroleum Geologists, Bakersfield, Calif.

Woodard, G. (1963), The Cenozoic succession of the West Colorado Desert, San Diego and Imperial Counties, Southern California, PhD thesis, Univ. of California, Berkeley, Calif.

Woodard, G. (1974), Redefinition of Cenozoic stratigraphic column in Split Mountain Gorge, Imperial Valley, California, *Am. Assoc. Pet. Geol. Bull.*, *58*(3), 521–539.

Yanites, B. J., G. E. Tucker, and R. S. Anderson (2009), Numerical and analytical models of cosmogenic radionuclide dynamics in landslide-dominated drainage basins, *J. Geophys. Res.*, *114*, F01007, doi:10.1029/2008JF001088.

Zachos, J., M. Pagani, L. Sloan, E. Thomas, and K. Billups (2001), Trends, rhythms, and aberrations in global climate 65 Ma to present, *Science*, *292*, 686–693.

Zhang, P., P. Molnar, and W. R. Downs (2001), Increased sedimentation rates and grain sizes 2–4 Myr ago due to the influence of climate change on erosion rates, *Nature*, *410*(6831), 891–897.